

Effective Boundary Conditions for Compressible Flows over Rough Boundaries

Giulia Deolmi , Wolfgang Dahmen and Siegfried Müller

Bericht Nr. 395

April 2014

Key words: homogenization; Navier wall law; compressible flow;
upscaling strategy; effective problem

AMS Subject Classifications: 74Q15, 76G25, 35Q30

**Institut für Geometrie und Praktische Mathematik
RWTH Aachen**

Templergraben 55, D-52056 Aachen, (Germany)

Giulia Deolmi, Wolfgang Dahmen, Siegfried Müller

Institut für Geometrie und Praktische Mathematik, RWTH Aachen, Templergraben 55 52056 Aachen,
Germany

{deolmi, dahmen, mueller}@igpm.rwth-aachen.de

EFFECTIVE BOUNDARY CONDITIONS FOR COMPRESSIBLE FLOWS OVER ROUGH BOUNDARIES

GIULIA DEOLMI

*Institut für Geometrie und Praktische Mathematik, RWTH Aachen, Templergraben 55
52056 Aachen, Germany
deolmi@igpm.rwth-aachen.de*

WOLFGANG DAHMEN

*Institut für Geometrie und Praktische Mathematik, RWTH Aachen, Templergraben 55
52056 Aachen, Germany
dahmen@igpm.rwth-aachen.de*

SIEGFRIED MÜLLER

*Institut für Geometrie und Praktische Mathematik, RWTH Aachen, Templergraben 55
52056 Aachen, Germany
mueller@igpm.rwth-aachen.de*

Simulations of a flow over a roughness are prohibitively expensive for small scale structures. If the interest is only on some macroscale quantity it will be sufficient to model the influence of the unresolved microscale effects. Such multiscale models rely on an appropriate upscaling strategy. Here the strategy originally developed by Achdou et al. ¹ for incompressible flows is extended to compressible high-Reynolds number flow. For proof of concept a laminar flow over a flat plate with partially embedded roughness is simulated. The results are compared with computations on a rough domain.

Keywords: Homogenization; Navier wall law; compressible flow; upscaling strategy; effective problem.

AMS Subject Classification: 74Q15, 76G25, 35Q30

1. Introduction

Domains with microscopic rough boundaries frequently arise in applications in engineering. For instance, small air injecting nozzles are used over wings of aircrafts to reduce the drag ³⁷. Examples can also be found in nature, e.g. the skin of sharks ²², and in everyday life, e.g. golf balls.

The challenge inherent in the numerical simulation of such problems is the high resolution that would be needed to resolve the roughness. In general, the computational costs will be prohibitively high and a simulation will not be feasible in spite of an ever increasing computer power. To deal with this type of problems we thus need concepts that allow us to quantify the influence of small scale effects on the

resolved macroscopic scale *without* resolving small scale structures. For this purpose concepts based on either *homogenization techniques*^{11,31,43}, (*heterogeneous*) *multiscale modeling*^{20,21} or multiscale finite element methods¹⁹ can be used. These concepts always need to be adapted to the problem at hand, i.e., for a given concrete application the main task is to derive an appropriate upscaling strategy.

We are particularly interested in *compressible* flows over a rough surface. A possible approach for the derivation of an appropriate upscaling strategy is to smooth artificially the boundary and solve the flow equations in the artificial smooth domain, cf.^{1,28}. Of course, this will introduce a significant error because micro-scale effects, due to the roughness, are discarded in this *zeroth order solution*. Therefore it has to be corrected by an appropriate correction term that depends on macro-scale *and* micro-scale variables. Plugging the modified solution into the original problem, another typically much simpler problem, the so-called *cell problem*, can be derived by means of an asymptotic expansion. In doing so one obtains also a correction for the boundary conditions on the artificial smooth surface where the solution of the cell problem enters. These are referred to as *effective boundary conditions* or *Navier wall laws*¹⁶ and can be considered as the upscaling model. Finally the effective problem can be solved on the smooth domain with the effective boundary conditions.

Previous related work addresses laminar and *incompressible* fluid flow modeled by the incompressible Navier-Stokes equations for moderate Reynolds numbers: in¹ a Navier wall law is derived applying homogenization techniques starting from a Taylor expansion of velocity and pressure where the zeroth order solution is first solved on an *extension* of the rough domain. In^{2,7,4} these ideas are extended to unsteady problems. In^{28,27} effective boundary conditions at the contact interface between a porous medium and a viscous incompressible fluid are derived. The corresponding asymptotic expansions have analogies with those in¹. However, instead of applying a Taylor expansion, a zeroth order approximation is computed first on a smooth *subset* of the rough domain and then it is continuously extended to the boundary of an effective domain *including* the roughness where it establishes the Navier wall law. This methodology is used in²² to solve a shape optimization problem, namely, finding the optimal “shape of the roughness” so as to minimize the drag force. Recently, this has been extended to turbulent incompressible flows, see²³.

A Navier wall law is derived also in^{13,14} for the steady Poisson problem, applying an idea similar to¹. In⁴⁴ similar ideas are applied to compute mass and momentum transfer over a rough surface, while in³ the authors try to derive boundary conditions on the artificial boundary using domain decomposition techniques. Finally there are also papers where the flow over rough walls is analyzed from an experimental point of view⁴².

The aim of this paper is to derive an upscaling strategy for the *compressible* flow regime for *high* Reynolds numbers. For this purpose we use some ideas presented in¹. However, here the underlying dynamics are much more complicated. Trans-

port effects are dominating dissipative effects due to viscosity and heat conduction. Moreover, boundary layers are much thinner and therefore more sensitive to perturbations. As a consequence some simplifications adopted in ¹ cannot be applied here and new ideas must be taken into account. In particular, for compressible flows the solution of the zeroth order approximation will enter the cell problem, so we must deal with a coupling between microscales and macroscales.

Although a complete rigorous foundation of our approach, as given in ^{27,28} for a different regime, is currently out of reach, the presented reasoning is supported by our numerical results which provide evidence of the effectiveness of our approach. The derivation of the cell problem uses asymptotic expansion arguments, different to classical perturbation theory ²⁵, in the course of which we carefully collect suitable “working hypotheses” which we argue are plausible but not theoretically founded.

The paper is organized as follows: in Section 2.1 we introduce the mathematical model based on the compressible Navier-Stokes equations and present the *effective problem* which is to capture the small scale effects on the macro scale. The core constituent of the effective problem are certain *effective boundary conditions* at the rough boundary. To identify such suitable boundary conditions we derive in Section 3 the cell problem by means of an asymptotic expansion. The solution of the cell problem is discussed in Section 4 where it is written in weak formulation. For proof of concept we investigate in Section 5 the laminar flow over a flat plate with partially embedded periodic roughness. The roughness elements are characterized by different heights and spacings. Of particular interest is the skin friction coefficient that serves as a measure for the quality of the effective model compared to simulations performed on the rough domain. We conclude in Section 6 with an outlook on future work.

2. Description of the problem

We are interested in the simulation of the flow over a rough surface where the roughness, characterized by its height ϵ , ranges on a scale that is by orders of magnitude smaller than other characteristic flow features, e.g., the boundary layer thickness δ . The different scales are referred to as the microscale and the macroscale, respectively. Since our main interest is on the understanding of the basic concepts to deal with this type of flow problems, we confine ourselves to the following simple two-dimensional configuration: let $\Omega^\epsilon \subset \mathbb{R}^2$ be a domain where its boundary $\partial\Omega^\epsilon$ is partly rough with periodic roughness elements of height ϵ and period s , see Figure 1 (left) for an illustration. The roughness is considered to be “small”, i.e., $x_2 = \epsilon h(x_1/\epsilon)$, rather than “shallow”, i.e., $x_2 = \epsilon h(x_1/\epsilon^{1+\beta})$, $\beta > 0$, see ³⁶. For vanishing roughness ϵ we obtain the smooth domain $\Omega^0 \supset \Omega^\epsilon$, as depicted in Figure 1 (right). These domains are characterized by the so-called *macroscale variable* $\mathbf{x} \in \mathbb{R}^2$. In contrast to the macroscale, the roughness is described by periodic roughness elements on the cell domain Y , see Figure 2, with Lipschitz boundary ∂Y . Any roughness element characterized by its position \bar{x}_1 in streamwise direction

is related to the macroscale by the *microscale variables* $\mathbf{y} \in Y$

$$\mathbf{y} := \frac{\mathbf{x} - \bar{x}_1 \mathbf{e}_1}{\epsilon} \quad (2.1)$$

for $\mathbf{x} \in \mathbb{R}^2$ with $x_1 \in [\bar{x}_1 - s/2, \bar{x}_1 + s/2]$.

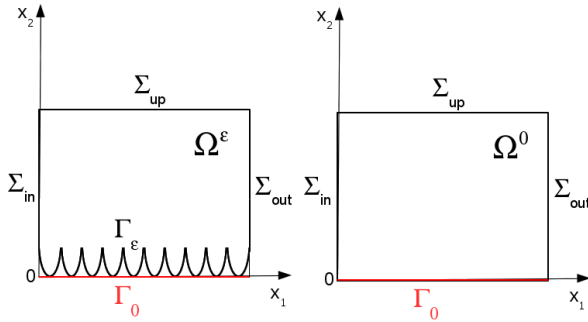


Fig. 1. Rough domain Ω^ϵ (left) and smooth domain Ω^0 (right).

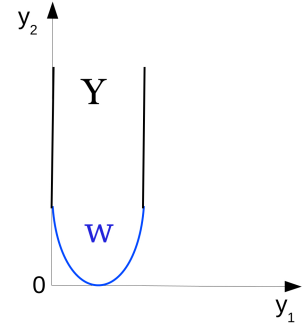


Fig. 2. Cell domain Y .

2.1. Mathematical model

The flow field in the rough domain Ω^ϵ is assumed to be compressible and time independent. Thus it is characterized by the steady compressible Navier-Stokes equations (NSE) composed of the balance laws for mass, momentum and total energy. In dimensionless form these read

$$\begin{aligned} \nabla \cdot (\rho \mathbf{u}) &= 0, \\ \nabla \cdot (\rho \mathbf{u} \otimes \mathbf{u}) + \nabla p &= \frac{1}{Re} \nabla \cdot \boldsymbol{\sigma}, \\ \nabla \cdot ((\rho E + p) \mathbf{u}) &= \frac{1}{Re} \nabla \cdot (\boldsymbol{\sigma} \mathbf{u} - \mathbf{q}), \end{aligned} \quad (2.2)$$

for the conserved quantities $(\rho, \rho \mathbf{u}, \rho E)$ with density ρ , velocity $\mathbf{u} = (u_1, u_2)$, pressure p and total energy $E = e + \frac{1}{2} \mathbf{u}^2$ composed of internal energy e and kinetic energy. The viscous stress tensor $\boldsymbol{\sigma}$ and the heat flux \mathbf{q} are defined for an isentropic Newtonian fluid by

$$\boldsymbol{\sigma} \equiv \boldsymbol{\sigma}(\mathbf{u}) = -\frac{2}{3} \eta (\nabla \cdot \mathbf{u}) \mathbb{I} + \eta (\nabla \mathbf{u} + (\nabla \mathbf{u})^T), \quad \mathbf{q} \equiv \mathbf{q}(T) = -\frac{\gamma}{Pr} \kappa \nabla T, \quad (2.3)$$

where we have used Fourier's law. Here η and κ denote the dimensionless dynamic shear viscosity coefficient and the heat conductivity coefficient, respectively, both assumed to be constant, and T the temperature. The system (2.2) is closed by the calorical and thermal equations of state for a perfect gas

$$e = T, \quad p = \rho e (\gamma - 1) = \rho RT \quad (2.4)$$

| | | | |
|------------------------|--------------------|----------------------------------|-------------------|
| length | \tilde{L}^* | \tilde{L}_{ref} | m |
| velocity | \tilde{u}^* | \tilde{u}_∞ | m/s |
| sound speed | \tilde{c}^* | \tilde{u}^* | m/s |
| time | \tilde{t}^* | \tilde{L}^*/\tilde{u}^* | s |
| density | $\tilde{\rho}^*$ | $\tilde{\rho}_\infty$ | kg/m ³ |
| pressure | \tilde{p}^* | $(\tilde{u}^*)^2 \tilde{\rho}^*$ | Pa |
| temperature | \tilde{T}^* | $(\tilde{u}^*)^2/\tilde{c}_v$ | K |
| energy | \tilde{e}^* | $(\tilde{u}^*)^2$ | J/kg |
| mass specific enthalpy | \tilde{h}^* | $(\tilde{u}^*)^2$ | J/kg |
| dynamic viscosity | $\tilde{\eta}^*$ | $\tilde{\eta}_\infty$ | kg/m s |
| heat conduction | $\tilde{\kappa}^*$ | $\tilde{\eta}^* \tilde{c}_p/Pr$ | J/m s K |
| specific gas constant | \tilde{R}^* | \tilde{c}_v | J/kg K |

Table 1. Reference values: \tilde{L}_{ref} is the characteristic length of the configuration and the quantities $(\)_\infty$ denote free-stream conditions.

with $\gamma = \tilde{c}_p/\tilde{c}_v$ the ratio of specific heats at constant pressure and volume, respectively. Moreover, $\tilde{c}_p = \tilde{c}_v + \tilde{R}$ is the specific gas constant where $\tilde{R} = R\tilde{c}_v$. For later use we also introduce the mass specific enthalpy h and the sound speed c which, for a perfect gas, read

$$h = e + p/\rho = \frac{p}{\rho} \frac{\gamma}{\gamma - 1}, \quad c^2 = \gamma p/\rho = \gamma RT. \quad (2.5)$$

The flow is characterized by the Reynolds number Re and the Prandtl number Pr

$$Re = \frac{\tilde{\rho}^* \tilde{u}^* \tilde{L}^*}{\tilde{\eta}^*}, \quad Pr = \frac{\tilde{\eta}^* \tilde{c}_p}{\tilde{\kappa}^*}$$

defined by reference values with dimensions indicated by the asterix. In Table 1 we summarize the reference values. Note that throughout this work we will use dimensionless quantities from which we can compute the corresponding quantities with dimensions, always indicated by a tilde, by multiplication with the respective reference quantity.

Throughout the remainder of this paper we will make the following assumptions.

Hypothesis: 2.1.

- (i) The flow is subsonic.
- (ii) The wall is adiabatic.

In particular, (i) implies that the Mach number $M = |\mathbf{u}|/c$ is less than one. Since in the subsonic flow regime no shocks develop due to compressibility effects, the solution of the problem is smooth. In particular, it allows us to consider the system (2.2), written in *conservative form*, in the equivalent *quasi-conservative form*

for the primitive variables $u := (\rho, \mathbf{u}, p)$, i.e., (2.2) becomes

$$\mathcal{L}(u) := \begin{pmatrix} (\mathbf{u} \cdot \nabla)\rho + \rho \nabla \cdot \mathbf{u} \\ (\mathbf{u} \cdot \nabla)\mathbf{u} + \frac{1}{\rho} \nabla p - \frac{1}{\rho Re} \nabla \cdot \boldsymbol{\sigma} \\ (\mathbf{u} \cdot \nabla)p + \gamma p (\nabla \cdot \mathbf{u}) + \frac{\gamma-1}{Re} ((\boldsymbol{\sigma} \cdot \nabla)\mathbf{u} + \nabla \cdot \mathbf{q}) \end{pmatrix} = 0, \quad (2.6)$$

where we employ the equation of state (2.4). Thus the solution $u^\epsilon = (\rho^\epsilon, \mathbf{u}^\epsilon, p^\epsilon)$ in the rough domain Ω^ϵ satisfies

$$\mathcal{L}(u^\epsilon) = 0 \quad \text{in } \Omega^\epsilon. \quad (2.7)$$

In view of Hypothesis 2.1, we impose at the various boundary portions of Ω^ϵ free-stream conditions $\rho_\infty, p_\infty, \mathbf{u}_\infty$, far-field conditions, outflow conditions characterized by the pressure p_{out} and adiabatic, no-slip conditions on $\Sigma_{in}, \Sigma_{up}, \Sigma_{out}$ and Γ_ϵ , respectively,

$$\begin{aligned} \rho^\epsilon &= \rho_\infty, \quad \frac{\partial p^\epsilon}{\partial n} = 0, \quad \mathbf{u}^\epsilon = \mathbf{u}_\infty \quad \text{on } \Sigma_{in}, \\ \frac{\partial \rho^\epsilon}{\partial n} &= 0, \quad p^\epsilon = p_\infty, \quad \mathbf{u}^\epsilon = \mathbf{u}_\infty \quad \text{on } \Sigma_{up}, \\ \frac{\partial \rho^\epsilon}{\partial n} &= 0, \quad p^\epsilon = p_{out}, \quad \frac{\partial \mathbf{u}^\epsilon}{\partial n} = 0 \quad \text{on } \Sigma_{out}, \\ \frac{\partial \rho^\epsilon}{\partial n} &= 0, \quad \frac{\partial p^\epsilon}{\partial n} = 0, \quad \mathbf{u}^\epsilon = \mathbf{0} \quad \text{on } \Gamma_\epsilon. \end{aligned} \quad (2.8)$$

We summarize for convenience these boundary conditions for the respective boundary portions as

$$\mathcal{R}_{in}(u^\epsilon) = 0, \quad \mathcal{R}_{up}(u^\epsilon) = 0, \quad \mathcal{R}_{out}(u^\epsilon) = 0. \quad (2.9)$$

In the following the problem (2.7), (2.8), respectively (2.9), is referred to as the *exact problem*. To our knowledge there is not much known about solvability and analytical properties of the solution to this problem. For regularity results for a similar problem on a polygon but only for Dirichlet boundary conditions, we refer to ³⁴.

Note that due to the perfect gas law (2.4) and $\frac{\partial p^\epsilon}{\partial n} = 0$ on Γ_ϵ , the adiabatic wall condition $\frac{\partial T^\epsilon}{\partial n} = 0$ implies $\frac{\partial \rho^\epsilon}{\partial n} = 0$ on Γ_ϵ and vice versa.

2.2. Zeroth order approximation

A simple but not very accurate approximation to the problem (2.7), (2.8) on the rough domain Ω^ϵ can be determined by solving the Navier-Stokes equations on the smooth domain $\Omega^0 \supset \Omega^\epsilon$, also shown in Figure 1, where we replace Γ_ϵ by Γ_0 in (2.8), i.e., the solution $u^0 = (\rho^0, \mathbf{u}^0, p^0)$ satisfies

$$\mathcal{L}(u^0) = 0 \quad \text{in } \Omega^0 \quad (2.10)$$

with boundary conditions

$$\begin{aligned} \mathcal{R}_{in}(u^0) &= 0, \quad \mathcal{R}_{out}(u^0) = 0, \quad \mathcal{R}_{up}(u^0) = 0, \\ \frac{\partial \rho^0}{\partial n} &= 0, \quad \frac{\partial p^0}{\partial n} = 0, \quad \mathbf{u}^0 = \mathbf{0}, \quad \text{on } \Gamma_0. \end{aligned} \quad (2.11)$$

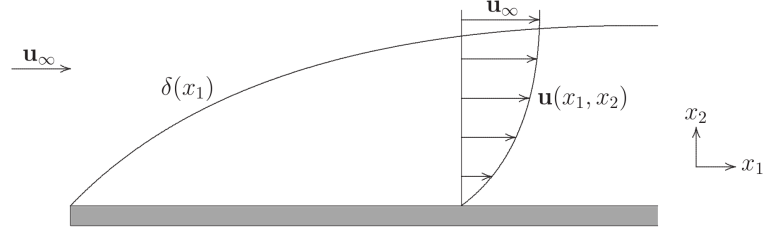


Fig. 3. Sketch of the zeroth order solution.

Due to the no-slip conditions on a smooth wall, all microscale effects are ignored so that its solution, referred to as *zeroth order approximation*, provides only a rough approximation to the exact solution. Nevertheless, in contrast to previous work in the low Reynolds number incompressible flow regime, the computation of zeroth-order solution is part of the proposed upscaling method. As long as the flow is laminar it is determined by a laminar boundary layer sketched in Figure 3 and a sufficiently accurate numerical solution requires, a much coarser resolution than the exact problem. Moreover, in simple model configurations as considered here it suffices to compute van Driest's similarity solution, ⁵.

2.3. Effective problem

To improve the accuracy of the zeroth order solution we have to account for the influence of the roughness on the macroscale, without resolving the microscale effects. Since in many applications the interest is on some averaged macroscale quantity, e.g. drag, the microscale effects due to the small scale structures need not to be resolved but their influence on the macroscale has to be properly modeled. Thus the idea is to replace the exact problem (2.7), (2.8) by an approximate problem in a smooth domain and to model the influence of the microscale effects on the macroscale quantities by imposing *appropriate boundary conditions* on the smooth boundary of yet another domain $\Omega^\sigma \subset \Omega^\epsilon$, see Figure 4, with smooth boundary Γ_σ . The so-called *effective problem* then reads

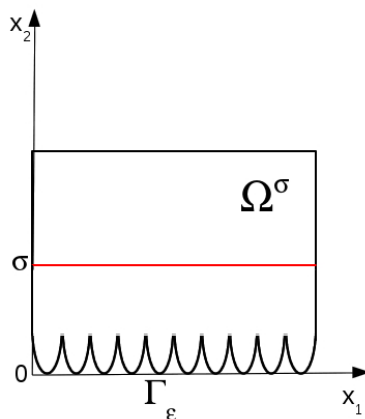
$$\mathcal{L}(u^{eff}) = 0 \quad \text{in } \Omega^\sigma \quad (2.12)$$

with boundary conditions

$$\begin{aligned} \mathcal{R}_{in}(u^{eff}) = 0, \quad \mathcal{R}_{out}(u^{eff}) = 0, \quad \mathcal{R}_{up}(u^{eff}) = 0, \\ \frac{\partial p^{eff}}{\partial n} = 0, \quad \frac{\partial p^{eff}}{\partial n} = 0, \quad \mathbf{u}^{eff} = \frac{\partial u_1^{eff}}{\partial x_2}(\sigma \mathbf{e}_1 + \epsilon \langle \boldsymbol{\chi} \rangle), \quad \text{on } \Gamma_\sigma. \end{aligned} \quad (2.13)$$

In contrast to Γ_0 , Γ_σ is located above the rough boundary Γ_ϵ , i.e., $\sigma \geq \epsilon$, but is still close to it, i.e., $\sigma = O(\epsilon)$. The distance σ from Γ_0 will be specified later.

Most importantly, we note that in the second line of (2.13), the no-slip conditions on Γ_ϵ in (2.8) have been replaced by the so-called *effective boundary conditions*, or

Fig. 4. Sketch of the domain Ω^σ .

Navier wall law, on Γ_σ . Here $\langle \chi \rangle \in \mathbb{R}^2$ is a constant that is computed by solving an auxiliary problem on the microscale, the so-called *cell problem*, modeling the microscale effect on the macroscale. The derivation of the Navier wall law and the choice of σ are in the focus of this work.

To this end, we proceed working under the following two further assumptions:

Hypothesis: 2.2.

- (i) The flow is laminar.
- (ii) Perturbations caused by the rough surface are only effective in the laminar boundary layer but have negligible influence outside this layer, i.e., $\epsilon \ll \delta$, see Fig. 3.

On account of Hypothesis 2.2, (i), the Reynolds number is in the range of 1×10^3 to 5×10^5 . In particular, the flow over a flat plate is parallel to the surface. And the boundary layer thickness can be approximated by $\delta \sim 1/\sqrt{Re}$.

Hypothesis 2.2, (ii) says that the roughness does not trigger any instationarity of the flow in the main stream.

3. Derivation of effective boundary conditions

In this section we derive the effective boundary conditions, i.e., the constant $\langle \chi \rangle$ in (2.13). For this purpose we use an upscaling strategy based on homogenization techniques. The underlying idea is an asymptotic expansion of the true solution u^ϵ of the exact problem (2.7), (2.8) in terms of ϵ powers, i.e.,

$$u^\epsilon(\mathbf{x}) = u^0(\mathbf{x}) + \epsilon u^1(\mathbf{x}, \mathbf{x}/\epsilon) + \mathcal{O}(\epsilon^2), \quad \mathbf{x} \in \Omega^\epsilon. \quad (3.1)$$

where u^0 is the (zeroth order) solution of (2.10). In view of Hypothesis 2.2, (ii), this expansion is supposed to hold only near the wall. We emphasize that in contrast

to classical perturbation theory, cf. ²⁵, the upscaling function u^1 depends on the macroscale variables *and* the microscale variables.

The modeling error introduced by the zeroth order solution has to be compensated by the upscaling function u^1 . In principle, plugging the asymptotic expansion (3.1) into the exact problem (2.7), (2.8), one can derive a system of partial differential equations for u^1 . However, solving the resulting system on Ω^ϵ would be as expensive as solving the exact problem. Instead, we make a “structured ansatz” for the upscaling function u^1 from which we derive a *cell problem* on the microscale with the aid of an asymptotic analysis. This latter reasoning makes use of the assumed regularity of the solution, see Hypothesis 2.2, (i). Averaging the solution of the cell problem will then give us the constant in the Navier wall law (2.13) for the effective problem (2.12). Thus, the derivation of u^1 is crucial to the overall modeling error.

3.1. Upscaling

Hypothesis 2.2, (ii) implies that the influence of the microscale on the macroscale will be dominant near the boundary but not in the far field. Therefore we first focus on the upscaling near the wall. In order to derive appropriate upscaling functions for the primitive variables, we evaluate the first order Taylor expansion of the zeroth order velocity \mathbf{u}^0 at $\mathbf{x} = (x_1, x_2) \in \Gamma_\epsilon$ on the rough boundary using its orthogonal projection $\mathbf{x}^0 = (x_1, 0)$ to Γ_0 as the expansion point, i.e.,

$$\mathbf{u}^0(x_1, x_2) = \mathbf{u}^0(x_1, 0) + \epsilon \frac{\partial \mathbf{u}^0}{\partial x_2}(x_1, 0) \frac{x_2}{\epsilon} + \mathcal{O}(\epsilon^2) = \epsilon \frac{\partial \mathbf{u}^0}{\partial x_2}(x_1, 0) \frac{x_2}{\epsilon} + \mathcal{O}(\epsilon^2), \quad (3.2)$$

where we have used that, due to the no-slip conditions (2.11), the velocity \mathbf{u}^0 vanishes at the wall Γ_0 . Note that, according to Figure 1 (right), $\Gamma_0 := \{(x_1, x_2) \in \Omega^0, x_2 = 0\}$, and that, since $\Omega^\epsilon \subset \Omega^0$, the solution of the zeroth order problem is defined on Γ_ϵ . Since by Hypothesis 2.2, (i), the velocity is parallel to Γ_0 , there is no flow in wall-normal direction which implies $\frac{\partial u_2^0}{\partial x_2} = 0$ in Ω^0 . Thus, introducing for ease of presentation

$$f(\mathbf{x}) = f(x_1, x_2) = f(x_1, 0) := \frac{\partial u_1^0}{\partial x_2}(x_1, 0),$$

we obtain for $\mathbf{x} = (x_1, x_2) \in \Gamma_\epsilon$

$$\mathbf{u}^0(x_1, x_2) = \epsilon \frac{\partial u_1^0}{\partial x_2}(x_1, 0) \mathbf{e}_1 \frac{x_2}{\epsilon} + \mathcal{O}(\epsilon^2) = \epsilon f(x_1, 0) \mathbf{e}_1 \frac{x_2}{\epsilon} + \mathcal{O}(\epsilon^2). \quad (3.3)$$

The term $\epsilon f(x_1, 0) \mathbf{e}_1 \frac{x_2}{\epsilon}$ can be considered as an approximation to the velocity of the zeroth order solution on the rough surface Γ_ϵ , where the leading term is the product of two factors $\epsilon f(x_1, 0)$ and $y_2 = \frac{x_2}{\epsilon}$ depending on macroscopic and microscopic variables, respectively. This motivates the following ansatz for the upscaling functions of the density, the velocity and the pressure

$$\begin{aligned} \rho^1(\mathbf{x}, \mathbf{y}) &:= f(x_1, 0) \phi(\mathbf{y}), \\ \mathbf{u}^1(\mathbf{x}, \mathbf{y}) &:= f(x_1, 0) \boldsymbol{\chi}(\mathbf{y}), \\ p^1(\mathbf{x}, \mathbf{y}) &:= f(x_1, 0) \pi(\mathbf{y}), \end{aligned} \quad (3.4)$$

where the *cell functions* ϕ , χ and π are assumed to be sufficiently smooth and only depend on the microscale. Later the cell functions will be determined by the solution of a *cell problem*, see Section 4.

We will make an upscaling ansatz for the effective solution of (2.12), (2.13) of the form

$$\rho^\epsilon = \rho^0 + \epsilon\rho^1 + \mathcal{O}(\epsilon^2), \quad \mathbf{u}^\epsilon = \mathbf{u}^0 + \epsilon\mathbf{u}^1 + \mathcal{O}(\epsilon^2), \quad p^\epsilon = p^0 + \epsilon p^1 + \mathcal{O}(\epsilon^2). \quad (3.5)$$

In order to investigate the upscaling error at the boundary we now plug the upscaling functions (3.4) into the expansion (3.1) of the exact solution $u^\epsilon = (\rho^\epsilon, \mathbf{u}^\epsilon, p^\epsilon)$. First, we consider the error in the velocity. For both, the exact problem and the zeroth order problem, no-slip conditions hold on the rough surface Γ_ϵ and on the smooth surface Γ_0 , respectively, i.e., $\mathbf{u}^\epsilon|_{\Gamma_\epsilon} = 0$ and $\mathbf{u}^0|_{\Gamma_0} = 0$ hold according to the boundary conditions (2.8) and (2.11). Hence, using (3.3) and (3.4), the upscaling error for the velocity at $\mathbf{x} = (x_1, x_2) \in \Gamma_\epsilon$ is given by

$$(\mathbf{u}^0 + \epsilon\mathbf{u}^1)(x_1, x_2) - \mathbf{u}^\epsilon(x_1, x_2) = \epsilon f(x_1, 0) \left(\mathbf{e}_1 \frac{x_2}{\epsilon} + \chi \right) + \mathcal{O}(\epsilon^2). \quad (3.6)$$

The upscaling errors for the first derivatives of the density and the pressure can be derived similarly. First of all, we note that

$$\left. \frac{\partial \rho^\epsilon}{\partial n} \right|_{\Gamma_\epsilon} = \left. \frac{\partial p^\epsilon}{\partial n} \right|_{\Gamma_\epsilon} = 0, \quad \left. \frac{\partial \rho^0}{\partial n} \right|_{\Gamma_0} = \left. \frac{\partial p^0}{\partial n} \right|_{\Gamma_0} = 0$$

hold because of the boundary conditions (2.8) and (2.11). As a consequence one has

$$\left. \frac{\partial^2 \rho^0}{\partial x_2 \partial x_1} \right|_{\Gamma_0} = \left. \frac{\partial^2 \rho^0}{\partial x_1 \partial x_2} \right|_{\Gamma_0} = \left. \frac{\partial^2 p^0}{\partial x_2 \partial x_1} \right|_{\Gamma_0} = \left. \frac{\partial^2 p^0}{\partial x_1 \partial x_2} \right|_{\Gamma_0} = 0.$$

Since f does not depend on x_2 and is determined by its values on the smooth boundary Γ_0 we have $\frac{\partial}{\partial x_2}(f(x_1, 0)) = 0$. Denoting by $\mathbf{n}(\mathbf{x}) = \mathbf{n} = (n_1, n_2)$ the outward normal at $\mathbf{x} \in \Gamma_\epsilon$ and \mathbf{x}^0 being the wall-normal projection of \mathbf{x} on Γ_0 and using Taylor expansions for ρ^0 and p^0 as well as the ansatz for the upscaling functions ρ^1 and p^1 , it follows that

$$\begin{aligned} \frac{\partial(\rho^0 + \epsilon\rho^1)}{\partial n}(\mathbf{x}) - \frac{\partial\rho^\epsilon}{\partial n}(\mathbf{x}) &= \left(\frac{\partial\rho^0}{\partial x_1}(\mathbf{x}^0) + \epsilon \frac{\partial f}{\partial x_1}(\mathbf{x}^0)\phi(\mathbf{x}) \right) n_1 + \\ &\quad \left(\epsilon \frac{\partial^2 \rho^0}{\partial x_2^2}(\mathbf{x}^0) \frac{x_2}{\epsilon} \right) n_2 + f(\mathbf{x}^0) \frac{\partial\phi}{\partial n}(\mathbf{x}), \end{aligned} \quad (3.7)$$

$$\begin{aligned} \frac{\partial(p^0 + \epsilon p^1)}{\partial n}(\mathbf{x}) - \frac{\partial p^\epsilon}{\partial n}(\mathbf{x}) &= \left(\frac{\partial p^0}{\partial x_1}(\mathbf{x}^0) + \epsilon \frac{\partial f}{\partial x_1}(\mathbf{x}^0)\pi(\mathbf{x}) \right) n_1 + \\ &\quad \left(\epsilon \frac{\partial^2 p^0}{\partial x_2^2}(\mathbf{x}^0) \frac{x_2}{\epsilon} \right) n_2 + f(\mathbf{x}^0) \frac{\partial\pi}{\partial n}(\mathbf{x}). \end{aligned} \quad (3.8)$$

In view of the asymptotic expansion (3.1), the cell functions ϕ , χ and π have to be chosen now in such a way that the expansion error is of order 2 near the wall Γ_ϵ , i.e., the leading terms on the right-hand sides in (3.6), (3.7) and (3.8) vanish.

3.2. Cell problem

The upscaling functions (3.4) are determined by the cell functions that only depend on the microscopic variables \mathbf{y} . In order to characterize the cell functions we plug (3.1) into the Navier-Stokes equations (2.7). When computing the derivatives with respect to the macroscopic variables \mathbf{x} we note that all quantities with respect to the zeroth order solution only depend on the macroscopic variables whereas the cell functions depend on the microscopic variables. The derivatives of the upscaling functions (3.4) are thus given by

$$\frac{\partial(\rho^0 + \epsilon\rho^1)}{\partial x_i} = \frac{\partial\rho^0}{\partial x_i} + f \frac{\partial\phi}{\partial y_i} + \mathcal{O}(\epsilon), \quad (3.9)$$

$$\frac{\partial(p^0 + \epsilon p^1)}{\partial x_i} = \frac{\partial p^0}{\partial x_i} + f \frac{\partial\pi}{\partial y_i} + \mathcal{O}(\epsilon), \quad (3.10)$$

$$\frac{\partial(\mathbf{u}^0 + \epsilon\mathbf{u}^1)}{\partial x_i} = \frac{\partial\mathbf{u}^0}{\partial x_i} + f \frac{\partial\boldsymbol{\chi}}{\partial y_i} + \mathcal{O}(\epsilon). \quad (3.11)$$

Therefore only the derivatives of the zeroth order solution and of the cell functions have to be taken into account.

In order to distinguish the derivatives with respect to \mathbf{x} and \mathbf{y} we will use ∇ , Δ and ∇_y , Δ_y , respectively. Since the calculations are tedious, we omit the details and only give the final results. From the continuity equation, the velocity equation and the pressure equation and using that the zeroth order solution satisfies (2.10), we derive

$$\begin{aligned} & \left((\mathbf{u}^0 \cdot \nabla_y)\phi + \rho^0 \nabla_y \cdot \boldsymbol{\chi} \right) f + \mathcal{O}(\epsilon) = 0, \\ & \left(\rho^0 (\mathbf{u}^0 \cdot \nabla_y)\boldsymbol{\chi} + \nabla_y \pi - \eta_\epsilon \left(\Delta_y \boldsymbol{\chi} + \frac{1}{3} \nabla_y (\nabla_y \cdot \boldsymbol{\chi}) \right) \right) f + \mathcal{O}(\epsilon) = 0, \\ & \left((\mathbf{u}^0 \cdot \nabla_y)\pi + \gamma p^0 \nabla_y \cdot \boldsymbol{\chi} - \frac{\kappa_\epsilon \gamma}{Pr \rho^0} \left(\Delta_y \pi - \frac{p^0}{\rho^0} \Delta_y \phi \right) \right) f + \mathcal{O}(\epsilon) = 0. \end{aligned} \quad (3.12)$$

Note that the zeroth order quantities $(\rho^0, \mathbf{u}^0, p^0)$ and the upscaling functions $(\phi, \boldsymbol{\chi}, \pi)$ are evaluated at the macroscale \mathbf{x} and the microscale \mathbf{x}/ϵ , respectively. Furthermore, the microscale dynamic shear viscosity coefficient and the microscale heat conductivity coefficient are defined as

$$\eta_\epsilon := \frac{\eta}{\epsilon Re}, \quad \kappa_\epsilon := \frac{\kappa}{\epsilon Re}. \quad (3.13)$$

In order to ensure at least first order accuracy in ϵ of the upscaling ansatz we choose the cell functions in such a way that the leading terms in (3.12) vanish, i.e.,

$$\begin{aligned} & (\mathbf{u}^0 \cdot \nabla_y)\phi + \rho^0 \nabla_y \cdot \boldsymbol{\chi} = 0 & \text{in } Y, \\ & \rho^0 (\mathbf{u}^0 \cdot \nabla_y)\boldsymbol{\chi} + \nabla_y \pi = \eta_\epsilon \left(\Delta_y \boldsymbol{\chi} + \frac{1}{3} \nabla_y (\nabla_y \cdot \boldsymbol{\chi}) \right) & \text{in } Y, \\ & (\mathbf{u}^0 \cdot \nabla_y)\pi + \gamma p^0 \nabla_y \cdot \boldsymbol{\chi} = \frac{\gamma \kappa_\epsilon}{Pr \rho^0} \left(\Delta_y \pi - \frac{p^0}{\rho^0} \Delta_y \phi \right) & \text{in } Y, \end{aligned} \quad (3.14)$$

should hold in a domain Y accommodating the microscale variables, referred to as cell domain, which in view of the relation $y_2 = x_2/\epsilon$, is *unbounded* in y_2 direction. see

Figure 2. We note that by $\rho^0, \mathbf{u}^0, p^0$ the cell problem, defined on the *microscale*, i.e., $(\phi, \chi, \pi) = (\phi(\mathbf{y}), \chi(\mathbf{y}), \pi(\mathbf{y}))$, is intertwined with the zeroth order solution $\rho^0(\mathbf{x}), \mathbf{u}^0(\mathbf{x}), p^0(\mathbf{x})$ on the *macroscale* $\mathbf{x} = \epsilon \mathbf{y} + \bar{x}_1 \mathbf{e}_1$.

To close the cell problem (3.14), we need to impose boundary conditions, in particular at the wall W , see Figure 2, on the microscale. For this purpose, we choose boundary conditions for χ such that the upscaling error (3.6) for the velocity becomes $\mathcal{O}(\epsilon^2)$, i.e., the leading term in (3.6) vanishes:

$$\chi(y_1, y_2) = -y_2 \mathbf{e}_1 \quad (y_1, y_2) \in W. \quad (3.15)$$

Similarly, requiring the following boundary conditions on ϕ and π ,

$$\begin{aligned} \frac{\partial u_1^0}{\partial x_2} \Big|_{\Gamma_0} \frac{\partial \phi}{\partial n} &= - \left(\frac{\partial \rho^0}{\partial x_1} \Big|_{\Gamma_0} + \epsilon \frac{\partial f}{\partial x_1} \phi \right) n_1 - \epsilon \frac{\partial^2 \rho^0}{\partial x_2^2} \Big|_{\Gamma_0} y_2 n_2, \\ \frac{\partial u_1^0}{\partial x_2} \Big|_{\Gamma_0} \frac{\partial \pi}{\partial n} &= - \left(\frac{\partial p^0}{\partial x_1} \Big|_{\Gamma_0} + \epsilon \frac{\partial f}{\partial x_1} \pi \right) n_1 - \epsilon \frac{\partial^2 p^0}{\partial x_2^2} \Big|_{\Gamma_0} y_2 n_2, \end{aligned} \quad (3.16)$$

on W , the errors (3.7) and (3.8) for the density and the pressure components, respectively, are reduced.

Since the roughness is assumed to be periodic, see Section 2.1, it is natural to impose periodic boundary conditions in streamwise direction, i.e.,

$$\chi, \phi, \pi \text{ are } s\text{-periodic}. \quad (3.17)$$

It will be shown numerically in Section 5.2, that the cell functions converge to some constant values for $y_2 \rightarrow \infty$. This motivates the following assumption:

Hypothesis: 3.1. The cell functions ϕ, χ and π converge for $y_2 \rightarrow \infty$ in the following sense: defining for the y_2 -cross sections $\Gamma_{up}^{y_2} = \{\bar{\mathbf{y}} \in Y : \bar{y}_2 = y_2\}$ with $y_2 \geq 1$, then the means are constant for $v \in \{\chi, \phi, \pi\}$, i.e.,

$$\frac{1}{|\Gamma_{up}^{y_2}|} \int_{\Gamma_{up}^{y_2}} v d\gamma = \langle v \rangle = \text{const} \quad \text{for } y_2 \geq 1 \quad (3.18)$$

and the functions are converging uniformly to the mean, i.e.,

$$\lim_{y_2 \rightarrow \infty} \|v|_{\Gamma_{up}^{y_2}} - \langle v \rangle\|_{\infty} = 0. \quad (3.19)$$

In the incompressible flow regime, Jäger and Mikelić verify in ^{26,28} for a Stokes cell problem that the means are independent of the y_2 -cross-sections $\Gamma_{up}^{y_2}$. Numerical computations verify that this holds true also for the above cell problem although it cannot be proven yet.

3.3. Effective problem

We emphasize that u^{eff} cannot be chosen as $u^0 + \epsilon u^1$ because determining u^1 would require solving a problem on Ω^ϵ . Instead, we want to set up an effective problem such that u^{eff} approximates u^ϵ on the lifted smooth boundary Γ_σ . For this purpose we need to specify the lifting parameter $\sigma \geq \epsilon$ and the effective boundary condition on Γ_σ . In a first step we therefore perform a Taylor expansion of \mathbf{u}^0 at $\mathbf{x} = (x_1, \sigma) \in \Gamma_\sigma$, in wall-normal direction similar to (3.2) where again we employ the no-slip condition of \mathbf{u}^0 at Γ_0 and laminarity of the flow field implying no flow in wall-normal direction, i.e., $u_2^0 \equiv 0$:

$$\mathbf{u}^0(x_1, \sigma) = \mathbf{u}^0(x_1, 0) + \sigma f(x_1, 0) \mathbf{e}_1 + \mathcal{O}(\sigma^2) = \sigma f(x_1, 0) \mathbf{e}_1 + \mathcal{O}(\epsilon^2). \quad (3.20)$$

Inserting this expansion in our asymptotic expansion (3.1) and using (3.4), we obtain

$$\begin{aligned} \mathbf{u}^\epsilon(x_1, \sigma) &= \mathbf{u}^0(x_1, \sigma) + \epsilon \mathbf{u}^1(\mathbf{x}, \mathbf{x}/\epsilon) + \mathcal{O}(\epsilon^2) \\ &= \mathbf{u}^0(x_1, \sigma) + \epsilon f(x_1, 0) \boldsymbol{\chi}(y_1, \sigma/\epsilon) + \mathcal{O}(\epsilon^2) \\ &= f(x_1, 0) (\sigma \mathbf{e}_1 + \epsilon \boldsymbol{\chi}(y_1, \sigma/\epsilon)) + \mathcal{O}(\epsilon^2). \end{aligned} \quad (3.21)$$

A natural choice for the effective problem then would be to choose the Dirichlet conditions

$$\mathbf{u}^{eff,1}(x_1, \sigma) = f(x_1, 0) (\sigma \mathbf{e}_1 + \epsilon \langle \boldsymbol{\chi} \rangle) \quad (3.22)$$

that are obtained substituting the function $\boldsymbol{\chi}(y_1, \sigma/\epsilon)$ by its mean $\langle \boldsymbol{\chi} \rangle$ at Γ_{up} . Instead of this, we consider the following Robin conditions

$$\mathbf{u}^{eff}(x_1, \sigma) = \frac{\partial u_1^{eff}}{\partial x_2}(x_1, \sigma) (\sigma \mathbf{e}_1 + \epsilon \langle \boldsymbol{\chi} \rangle) \quad (3.23)$$

that do not depend explicitly on \mathbf{u}^0 but the zeroth order solution only enters implicitly via the mean $\langle \boldsymbol{\chi} \rangle$ of the cell solution.

We now introduce the errors

$$\mathbf{e}^{eff,1}(x_1, \sigma) := \mathbf{u}^\epsilon(x_1, \sigma) - \mathbf{u}^{eff,1}(x_1, \sigma), \quad (3.24)$$

$$\mathbf{e}^{eff}(x_1, \sigma) := \mathbf{u}^\epsilon(x_1, \sigma) - \mathbf{u}^{eff}(x_1, \sigma). \quad (3.25)$$

By means of (3.21), (3.22) and (3.23) these errors can be written as

$$\begin{aligned} \mathbf{e}^{eff,1}(x_1, \sigma) &= \epsilon f(x_1, 0) (\boldsymbol{\chi}(y_1, \sigma/\epsilon) - \langle \boldsymbol{\chi} \rangle) + \mathcal{O}(\epsilon^2) \\ \mathbf{e}^{eff}(x_1, \sigma) &= \mathbf{e}^{eff,1} + \left(\frac{\partial u_1^0}{\partial x_2}(x_1, 0) - \frac{\partial u_1^{eff}}{\partial x_2}(x_1, \sigma) \right) (\sigma \mathbf{e}_1 + \epsilon \langle \boldsymbol{\chi} \rangle). \end{aligned} \quad (3.26)$$

Since numerical computations confirm that $|\langle \boldsymbol{\chi}_2 \rangle| \ll |\langle \boldsymbol{\chi}_1 \rangle|$, we choose the smallest admissible $\sigma \geq \epsilon$ such that $\sigma + \epsilon \langle \boldsymbol{\chi}_1 \rangle$ is minimized, i.e. $\sigma = \epsilon$, to get as close as possible to $\mathbf{e}^{eff,1}$. Note that the error $\mathbf{e}^{eff,1}$ is of order $\mathcal{O}(\epsilon)$ for small σ but of higher order $\mathcal{O}(\epsilon^\alpha)$, $\alpha > 1$, for large σ , because $\boldsymbol{\chi}(y_1, \sigma/\epsilon)$ tends (numerically) to $\langle \boldsymbol{\chi} \rangle$ for $\sigma \rightarrow \infty$. On the other hand, the second term in \mathbf{e}^{eff} might also become small because u^{eff} tends (numerically) to u^0 for $\epsilon \rightarrow 0$.

3.4. Some remarks

We briefly relate the present approach to previous work. Note that in the context of a Poisson problem, Bresch and Milisic in ^{13,14} introduce a multiscale wall-law which consists in considering a pointwise value in the effective law. Alternatively one can use the mean value $\langle \chi \rangle$ instead of the point value χ , as done in ^{1,2,28,27} and motivated by the Beavers-Joseph experiment ⁹. This approach is adopted also in this paper.

The upscaling strategy presented in the previous sections is motivated by earlier work of Achdou et al., cf. ¹, in the *incompressible* flow regime. Since we are dealing with *compressible* flows the free-stream velocities imposed at the inflow boundary are significantly larger causing non-negligible density variations in the boundary layer. This strongly affects the cell problem. First of all, we may no longer neglect the influence of the zeroth order solution in the cell problem as done in ¹. In Section 5.2 we will investigate by means of numerical simulations that these terms have a significant influence on the effective constants in the compressible case. Furthermore we also have to solve equations for the cell functions ϕ and π for the density and the pressure, respectively. Thus we need additional boundary conditions for these functions as well. This results in a system of partial differential equations where in addition to dissipative effects, as in ¹, we also have to account for transport effects that typically complicates its numerical discretization.

A crucial question is where to pose the effective boundary conditions. A first approach considered in ¹ is

$$\mathbf{u}^{eff} = \epsilon \frac{\partial u_1^0}{\partial x_2} \langle \chi \rangle, \text{ on } \Gamma_0. \quad (3.27)$$

Since this requires the knowledge of the zeroth order solution, in a second approach it was suggested to replace (3.27) by

$$\mathbf{u}^{eff} = \epsilon \frac{\partial u_1^{eff}}{\partial x_2} \langle \chi \rangle, \text{ on } \Gamma_0. \quad (3.28)$$

Thus, the Dirichlet condition becomes now a Robin condition. Since $\langle \chi \rangle$ is negative, as confirmed by computations, (3.27) and (3.28) impose a counterflow at the wall, opposed to the flow outside the boundary layer. Therefore a vortex develops, located in a thin layer of height proportional to ϵ , i.e., the effective problem still needs to resolve micro-scale effects. This has been confirmed numerically for approach (3.27). For approach (3.28) it turned out that the computation becomes numerically unstable, when the thin layer is resolved too well. From a theoretical point of view, it has been shown in ¹ for the incompressible case that the effective problem corresponding to (3.28) does not satisfy the Lax-Milgram Theorem. Therefore Achdou et al. finally suggested a third approach

$$\mathbf{u}^{eff} = \epsilon \frac{\partial u_1^{eff}}{\partial x_2} (\langle \chi \rangle + \delta \mathbf{e}_1), \text{ on } \Gamma_\delta, \quad (3.29)$$

where $\delta > 0$ is chosen such that $\langle \chi_1 \rangle + \delta$ is positive, so that the weak formulation of the effective problem has a unique solution. The derivation is similar to (3.21) performing a Taylor expansion of u_1^0 on Γ_0 instead of Γ_σ . Choosing, in particular, $\sigma = \delta\epsilon$ in (2.13) then the effective boundary conditions coincide with (3.29). There is no strategy presented in ¹ how to choose σ .

Alternatively, Jäger and Mikelić ²⁸ consider the effective boundary conditions

$$\mathbf{u}^{eff} = -\epsilon \frac{\partial u_1^{eff}}{\partial x_2} \langle \chi \rangle, \text{ on } \Gamma_\sigma. \quad (3.30)$$

These coincide with (2.13) if $\sigma = -2\epsilon \langle \chi_1 \rangle \geq 0$.

Observe that for both approaches (3.29) and (3.30) the constants $\langle \chi_1 \rangle + \delta$ and $-\langle \chi_1 \rangle$, respectively, are positive. Hence, there is no counterflow induced at the wall and no vortex develops, i.e., there is no need to resolve an effect on a micro-scale grid resolution and numerical instabilities no longer occur for the upscaled problem.

4. Solution of the cell problem

In Section 3.2 the cell problem (3.14) together with its boundary conditions (3.15), (3.16) and (3.17) has been derived on an *unbounded* domain in wall-normal direction, see Figure 2. Since by Hypothesis (3.1) the solution of the cell problem is supposed to converge in wall-normal direction, we may truncate the domain Y by a fixed cross section Γ_{up} choosing the corresponding y_2 large enough to ensure that $\phi|_{\Gamma_{up}}$, $\chi|_{\Gamma_{up}}$ and $\pi|_{\Gamma_{up}}$ are almost converged to the mean value according to Hypothesis 3.1 within $\mathcal{O}(\epsilon^2)$ and define the averages at Γ_{up}

$$\langle \phi \rangle := \frac{1}{|\Gamma_{up}|} \int_{\Gamma_{up}} \phi d\gamma, \quad \langle \chi \rangle := \frac{1}{|\Gamma_{up}|} \int_{\Gamma_{up}} \chi d\gamma, \quad \langle \pi \rangle := \frac{1}{|\Gamma_{up}|} \int_{\Gamma_{up}} \pi d\gamma. \quad (4.1)$$

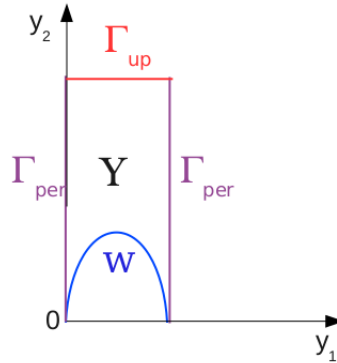


Fig. 5. Bounded cell domain Y .

When bounding the domain in wall-normal direction by Γ_{up} , see Figure 5, we have to prescribe additional boundary conditions on Γ_{up} . As it is motivated later on when considering the weak formulation of the cell problem, we use Robin type and von Neumann type boundary conditions for χ and ϕ , respectively, i.e.,

$$(\eta_\epsilon \nabla \chi - \pi \mathbb{I}) \mathbf{n} = \mathbf{0}, \quad \nabla \phi \cdot \mathbf{n} = 0 \quad \text{on } \Gamma_{up}. \quad (4.2)$$

4.1. Weak formulation

In order to solve the cell problem (3.14) together with its boundary conditions (3.15), (3.16), (3.17), and (4.2) it will be convenient to reformulate it somewhat as follows. By the first equation in (3.14) we have $\nabla_y \cdot \chi = -\frac{1}{\rho^0}(\mathbf{u}^0 \cdot \nabla_y)\phi$. A corresponding substitution of $\nabla_y \cdot \chi$ in the momentum and pressure equation in (4.2), yields to the equivalent (strong) system

$$\begin{aligned} (\mathbf{u}^0 \cdot \nabla_y)\phi + \rho^0 \nabla_y \cdot \chi &= 0 && \text{in } Y, \\ \rho^0 (\mathbf{u}^0 \cdot \nabla_y)\chi + \nabla_y \pi &= \eta_\epsilon \left(\Delta_y \chi - \frac{1}{3} \nabla_y \left(\frac{1}{\rho^0} (\mathbf{u}^0 \cdot \nabla_y)\phi \right) \right) && \text{in } Y, \\ (\mathbf{u}^0 \cdot \nabla_y)\pi - \gamma \frac{\rho^0}{Pr} (\mathbf{u}^0 \cdot \nabla_y)\phi &= \frac{\gamma \kappa_\epsilon}{Pr \rho^0} \left(\Delta_y \pi - \frac{\rho^0}{\rho^0} \Delta_y \phi \right) && \text{in } Y, \end{aligned} \quad (4.3)$$

subject to the same boundary conditions as before. To solve this system numerically with the aid of finite element discretizations we need to derive suitable weak formulations. It suffices to ensure unique solvability for homogeneous boundary conditions for χ . As trial spaces we choose the following infinite dimensional spaces:

$$\mathbf{V}_\chi := \mathbf{H}_{0,W,per}^1(Y), \quad V_\phi = V_\pi := H_{per}^1(Y), \quad (4.4)$$

where $H_{0,D}^1(Y)$ denotes the space of functions of $H^1(Y)$ that are zero on $D \subset \partial Y$, and where the subscript “*per*” indicates periodicity in the y_1 -coordinate, that is the traces on opposite side walls Γ_{per} coincide. Moreover, the test spaces are chosen to be identical to the trial spaces, i.e., we seek a weak formulation over $\mathbf{V} \times \mathbf{V}$, where $\mathbf{V} = \mathbf{V}_\chi \times \mathbf{V}_\phi \times \mathbf{V}_\pi$.

We first test the continuity equation in (3.14) by the test function $v_\phi \in V_\phi$ to obtain its weak formulation

$$b_\phi([\phi, \chi], v_\phi) := \int_Y v_\phi (\mathbf{u}^0 \cdot \nabla_y)\phi + v_\phi \rho^0 \nabla_y \cdot \chi dy = 0, \quad v_\phi \in V_\phi. \quad (4.5)$$

Consider now the momentum equation. Note that, due to the boundary conditions (4.2),

$$\int_{\partial Y} \mathbf{n} \cdot \mathbf{v}_\chi \pi - \eta_\epsilon \mathbf{v}_\chi \cdot \nabla_y \chi \mathbf{n} d\gamma = \int_{\Gamma_{up}} \mathbf{v}_\chi \pi \cdot \mathbf{n} - \eta_\epsilon \mathbf{v}_\chi \cdot \nabla_y \chi \cdot \mathbf{n} d\gamma = 0$$

holds for all $\mathbf{v}_\chi \in \mathbf{V}_\chi$. Thus, testing the momentum equation in (4.3) by the test function $\mathbf{v}_\chi \in \mathbf{V}_\chi$, we obtain after some calculations

$$\begin{aligned}
 b_\chi([\phi, \chi, \pi], \mathbf{v}_\chi) &:= \int_Y \left(\mathbf{v}_\chi \cdot \rho^0 (\mathbf{u}^0 \cdot \nabla_y) \chi + \eta_\epsilon \nabla_y \mathbf{v}_\chi : \nabla_y \chi \right. \\
 &\quad \left. - \int_Y \left(\frac{\eta_\epsilon}{3\rho^0} (\nabla_y \cdot \mathbf{v}_\chi) (\mathbf{u}^0 \cdot \nabla_y \phi) + (\nabla_y \cdot \mathbf{v}_\chi) \pi \right) dy \right. \\
 &\quad \left. + \int_{\Gamma_{up}} \frac{\eta_\epsilon}{3\rho^0} \mathbf{v}_\chi \cdot \mathbf{n} (\mathbf{u}^0 \cdot \nabla_y \phi) d\gamma, \quad \mathbf{v}_\chi \in \mathbf{V}_\chi, \right. \quad (4.6)
 \end{aligned}$$

where

$$\nabla_y \mathbf{v} : \nabla_y \psi := \sum_{i,j=1,2} \frac{\partial v_i}{\partial y_j} \frac{\partial \psi_i}{\partial y_j},$$

and where we have used that by periodicity and the definition of \mathbf{V}_χ and V_ϕ ,

$$\int_{\partial Y} \frac{\eta_\epsilon}{3\rho^0} \mathbf{v}_\chi (\mathbf{u}^0 \cdot \nabla_y) \phi \cdot \mathbf{n} d\gamma = \int_{\Gamma_{up}} \frac{\eta_\epsilon}{3\rho^0} \mathbf{v}_\chi (\mathbf{u}^0 \cdot \nabla_y) \phi \cdot \mathbf{n} d\gamma.$$

Finally, we treat the pressure equation in (4.3) in an analogous fashion and test it with the test function $v_\pi \in V_\pi$. We note first, that due to the conditions on the derivatives of pressure and density (3.16), the following relation holds.

$$\begin{aligned}
 &\int_W \frac{\gamma \kappa_\epsilon}{Pr \rho^0} v_\pi \left(-\nabla_y \pi \cdot \mathbf{n} + \frac{p^0}{\rho^0} \nabla_y \phi \cdot \mathbf{n} \right) d\gamma = \\
 &\int_W \frac{\gamma \kappa_\epsilon}{Pr \rho^0} \frac{\partial u_1^0}{\partial x_2} \Big|_{\Gamma_0} v_\pi \epsilon \frac{\partial^2 u_1^0}{\partial x_1 \partial x_2} \Big|_{\Gamma_0} n_1 \left(\pi - \frac{p^0}{\rho^0} \phi \right) d\gamma + \\
 &\int_W \frac{\gamma \kappa_\epsilon}{Pr \rho^0} \frac{\partial u_1^0}{\partial x_2} \Big|_{\Gamma_0} v_\pi \left[n_1 \left(\frac{\partial p^0}{\partial x_1} \Big|_{\Gamma_0} - \frac{p^0}{\rho^0} \frac{\partial \rho^0}{\partial x_1} \Big|_{\Gamma_0} \right) \right. \\
 &\quad \left. + \epsilon y_2 n_2 \left(\frac{\partial^2 p^0}{\partial x_2^2} \Big|_{\Gamma_0} - \frac{p^0}{\rho^0} \frac{\partial^2 \rho^0}{\partial x_2^2} \Big|_{\Gamma_0} \right) \right] d\gamma.
 \end{aligned}$$

Moreover, since $v_\pi \in V_\pi$, boundary terms agree on both components of Γ_{per} and, due to the orientation of the respective normals, cancel. Imposing the von Neumann boundary condition $\nabla \phi \cdot \mathbf{n} = 0$, see (4.2), only one boundary integral term on Γ_{up} remains in the weak formulation. Thus, abbreviating for convenience

$$\begin{aligned}
 q^0 &:= \frac{p^0}{\rho^0}, & C_0 &:= \frac{\gamma \kappa_\epsilon}{Pr \rho^0}, & p_1^0 &:= \frac{\partial p^0}{\partial x_1} \Big|_{\Gamma_0}, & p_{1,2}^0 &:= \frac{\partial^2 p^0}{\partial x_2^2} \Big|_{\Gamma_0}, \\
 u_2^0 &:= \left(\frac{\partial u_1^0}{\partial x_2} \Big|_{\Gamma_0} \right)^{-1}, & u_{1,2}^0 &:= \frac{\partial^2 u_1^0}{\partial x_1 \partial x_2} \Big|_{\Gamma_0}, & \rho_1^0 &:= \frac{\partial \rho^0}{\partial x_1} \Big|_{\Gamma_0}, & \rho_{1,2}^0 &:= \frac{\partial^2 \rho^0}{\partial x_2^2} \Big|_{\Gamma_0},
 \end{aligned}$$

after some calculations we finally end up with

$$\begin{aligned}
b_\pi([\phi, \boldsymbol{\chi}, \pi], v_\pi) &:= \int_Y v_\pi(\mathbf{u}^0 \cdot \nabla_y) \pi - v_\pi \gamma q^0(\mathbf{u}^0 \cdot \nabla_y) \phi + \nabla_y(C_0 v_\pi) \cdot \nabla_y \pi \\
&\quad - \nabla_y(C_0 q^0 v_\pi) \cdot \nabla_y \phi dy - \int_{\Gamma_{up}} C_0 v_\pi \nabla_y \pi \cdot \mathbf{n} d\gamma \\
&\quad + \int_W \epsilon(C_0 u_2^0 u_{1,2}^0 n_1) (\pi - q^0 \phi) v_\pi d\gamma \tag{4.7} \\
&= - \int_W C_0 u_2^0 [n_1(p_1^0 - q^0 \rho_1^0) + \epsilon y_2 n_2(p_{1,2}^0 - q^0 \rho_{1,2}^0)] v_\pi d\gamma
\end{aligned}$$

for $v_\pi \in V_\pi$.

We consider now the bilinear form for $\mathbf{U} = (\boldsymbol{\chi}, \phi, \pi)$, $\mathbf{V} = (v_\chi, v_\phi, v_\pi)$ defined by

$$\begin{aligned}
b(\mathbf{U}, \mathbf{V}) &:= b_\phi([\phi, \boldsymbol{\chi}], v_\phi) + b_\chi([\phi, \boldsymbol{\chi}, \pi], v_\chi) + b_\pi([\phi, \boldsymbol{\chi}, \pi], v_\pi) \\
&= \int_Y v_\phi(\mathbf{u}^0 \cdot \nabla_y) \phi + v_\phi \rho^0 \nabla_y \cdot \boldsymbol{\chi} dy \\
&\quad + \int_Y v_\chi \cdot \rho^0(\mathbf{u}^0 \cdot \nabla_y) \boldsymbol{\chi} - (\nabla_y \cdot v_\chi) \pi \\
&\quad + \eta_\epsilon \nabla_y v_\chi : \nabla_y \boldsymbol{\chi} - \frac{\eta_\epsilon}{3\rho^0} (\nabla_y \cdot v_\chi) (\mathbf{u}^0 \cdot \nabla_y) \phi dy \\
&\quad + \int_{\Gamma_{up}} \frac{\eta_\epsilon}{3\rho^0} v_\chi(\mathbf{u}^0 \cdot \nabla_y) \phi \cdot \mathbf{n} d\gamma \\
&\quad + \int_Y v_\pi(\mathbf{u}^0 \cdot \nabla_y) \pi - v_\pi \gamma q^0(\mathbf{u}^0 \cdot \nabla_y) \phi + C_0 \nabla_y v_\pi \cdot \nabla_y \pi \\
&\quad - q^0 C_0 \nabla_y v_\pi \cdot \nabla_y \phi dy - \int_{\Gamma_{up}} C_0 v_\pi \nabla_y \pi \cdot \mathbf{n} d\gamma \\
&\quad + \int_W \epsilon C_0 u_2^0 u_{1,2}^0 n_1 (\pi - q^0 \phi) v_\pi d\gamma
\end{aligned}$$

so that the weak formulation of the cell problem reads: find $\mathbf{U} = (\boldsymbol{\chi}, \phi, \pi) \in V_\phi \times \mathbf{V}_\chi \times V_\pi$ such that for each $\mathbf{V} = (v_\phi, v_\chi, v_\pi) \in V_\phi \times \mathbf{V}_\chi \times V_\pi$ one has

$$b(\mathbf{U}, \mathbf{V}) = F(\mathbf{V}) = F_\pi(v_\pi), \tag{4.8}$$

where

$$F_\pi(v_\pi) = - \int_W C_0 u_2^0 [n_1(p_1^0 - q^0 \rho_1^0) + \epsilon y_2 n_2(p_{1,2}^0 - q^0 \rho_{1,2}^0)] v_\pi d\gamma.$$

We observe next that (4.7) can be written as the difference of two very similar

elliptic problems. Specifically, consider

$$\begin{aligned}
 b_{\pi,\pi}(\pi, v_\pi) &:= \int_Y ((\mathbf{u}^0 \cdot \nabla_y) \pi v_\pi + C_0 \nabla_y \pi \cdot \nabla_y v_\pi) dy \\
 &\quad - \int_{\Gamma_{up}} C_0 v_\pi \nabla_y \pi \cdot \mathbf{n} d\gamma + \int_W \epsilon (C_0 u_2^0 u_{1,2}^0 n_1) \pi v_\pi d\gamma \\
 &= - \int_W C_0 u_2^0 [n_1 p_1^0 + \epsilon y_2 n_2 p_{1,2}^0] v_\pi d\gamma, \quad v_\pi \in V_\pi, \quad (4.9)
 \end{aligned}$$

as well as

$$\begin{aligned}
 b_{\pi,\phi}(\phi, v_\pi) &= \int_Y -\gamma q^0 ((\mathbf{u}^0 \cdot \nabla_y) \phi) v_\pi - C_0 q^0 \nabla_y v_\pi \cdot \nabla_y \phi dy \\
 &\quad - \int_W \epsilon (C_0 u_2^0 u_{1,2}^0 n_1) q^0 \phi v_\pi d\gamma \\
 &= + \int_W C_0 u_1^0 [n_1 q^0 \rho_1^0 + \epsilon y_2 n_2 q^0 \rho_{1,2}^0] v_\pi d\gamma, \quad v_\pi \in V_\pi. \quad (4.10)
 \end{aligned}$$

Thus, (4.9) and (4.10) are convection diffusion equations which subject to the given boundary conditions have unique solutions in $V_\pi = V_\phi$. Observe moreover that $b_\chi([\phi, \chi, \pi], \mathbf{v}_\chi)$ is again an elliptic form in χ which has a unique solution for given π, ϕ . Here we have to assume that ϕ is actually regular enough to ensure that $\mathbf{u}^0 \cdot \nabla_y \phi$ belongs to $H^{-1/2}(\Gamma_{up})$. This shows existence.

5. Laminar flow over a rough plate

For a proof of concept we consider a laminar flow of a compressible fluid over a flat plate with *partially* embedded roughness. This allows to perform numerical simulations of the exact problem that can be compared with the solution of the effective problem to provide inside on the modeling error. Furthermore, the zeroth order approximation coincides with the flow over a flat plate that can be approximated by van Driest's similarity solution.

The configuration with and without partial roughness are sketched in Figure 6. Following the notation in Figure 1 the smooth domain is determined by $\Omega^\sigma := [-0.0125, 2.5] \times [\sigma, 0.0375]$ with boundaries

$$\begin{aligned}
 \Sigma_{in} &:= \{0\} \times [0, 0.0375] \cup [-0.125, 0] \times \{0\}, \\
 \Sigma_{up} &:= [-0.125, 2.5] \times \{0.0375\}, \\
 \Sigma_{out} &:= \{2.5\} \times [0, 0.0375], \\
 \Sigma_0 &:= [0, 0.875] \times \{0\} \cup [1, 2.5] \times \{0\}, \\
 \Sigma_{sym} &:= [-0.0125, 0] \times \{0\}, \\
 \Sigma_\sigma &:= [0, 0.875] \times \{\sigma\} \cup [1, 2.5] \times \{\sigma\}, \\
 \Gamma_\sigma &:= [0.875, 1] \times \{\sigma\} \\
 \Sigma_{sym,\sigma} &:= [-0.0125, 0] \times \{\sigma\}.
 \end{aligned}$$

For the domain Ω^ϵ , we replace the boundary Γ_0 by Γ_ϵ with roughness structure described below.

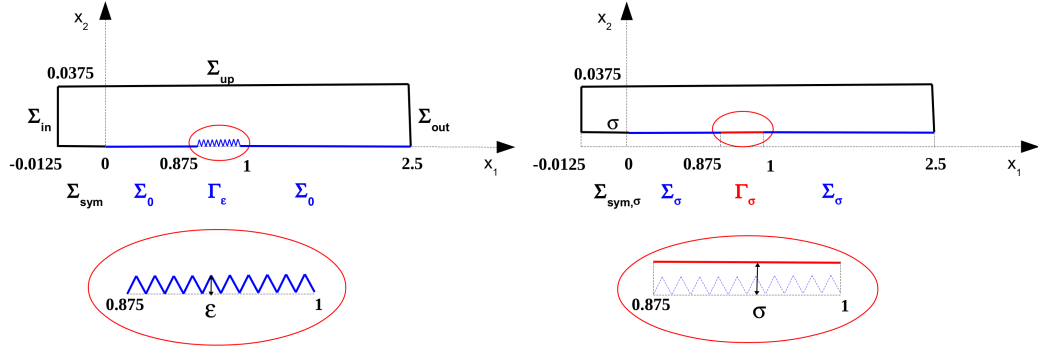


Fig. 6. Test case: configuration of a flat plate with (left) and without (right) roughness.

The flow field is characterized by the Reynolds number $Re_\infty = 5 \cdot 10^5$. In the viscous stress tensor and the heat flux, see equation (2.3), the dynamic viscosity coefficient and the heat conductivity coefficient are chosen as $\eta = 1$ and $\kappa = 1$, respectively. The gas is assumed to be air, thus we use $Pr = 0.72$ for the Prandtl number and $\gamma = 1.4$ for the ratio of specific heats.

The free-stream conditions are characterized by the free-stream Mach number $M_\infty = |u_\infty|/c_\infty = 0.3$ with $c_\infty^2 = \gamma p_\infty/\rho_\infty = \gamma RT$. According to the reference values given in Table 1 we conclude

$$\rho_\infty = 1, \quad \mathbf{u}_\infty = (1, 0)^T, \quad p_\infty = \frac{1}{M_\infty^2 \gamma}.$$

Since for the flow solver at hand we have to specify the quantities with dimensions, for convenience of the reader we give the reference length $\tilde{L}_{ref} = 0.08$ m and the free-stream values for temperature $\tilde{T}_\infty = 293$ K, dynamic viscosity $\tilde{\eta}_\infty = 1.8 \cdot 10^{-5}$ kg/m s, speed of sound $\tilde{c}_\infty = (\gamma \tilde{R} \tilde{T}_\infty)^{1/2} = 337.16$ s, velocity $\tilde{u}_\infty = M_\infty \tilde{c}_\infty = 101.15$ m/s, density $\tilde{\rho}_\infty = Re \tilde{\eta}_\infty / \tilde{u}_\infty L^* = 1.11$ kg/m³ as well as the specific heat $\tilde{c}_v = 692.83$ J/kg K and the specific gas constant $\tilde{R} = \tilde{c}_p - \tilde{c}_v = 277.13333$ J/kg K for air.

5.1. Approximation of the zeroth order solution

For computing the solution of the cell problem (3.14) together with its boundary conditions (3.15), (3.16), (3.17) and (4.2) or the corresponding variational problem (4.8), we need as input the quantities $(\rho^0, \mathbf{u}^0, p^0)$ evaluated near the smooth wall

Γ_0 and the derivatives at Γ_0

$$\left. \frac{\partial u_1^0}{\partial x_2} \right|_{\Gamma_0}, \quad \left. \frac{\partial^2 p^0}{\partial x_2^2} \right|_{\Gamma_0}, \quad \left. \frac{\partial^2 \rho^0}{\partial x_2^2} \right|_{\Gamma_0}, \quad \left. \frac{\partial \rho^0}{\partial x_1} \right|_{\Gamma_0}, \quad \left. \frac{\partial^2 u_1^0}{\partial x_1 \partial x_2} \right|_{\Gamma_0},$$

determined by the zeroth order problem (2.10) with its boundary conditions (2.11).

To avoid performing the numerical computation of the zeroth order solution we employ van Driest's similarity solution that can be derived from the boundary layer theory for laminar compressible fluid flow over a flat plate, cf. ⁵. This is admissible as long as $\frac{1}{Re} = \mathcal{O}(\delta^2)$ holds true, where δ denotes the dimensionless boundary layer thickness, ⁵, i.e., the flow remains laminar. To be consistent with our assumption that the effects of the roughness stay all inside the boundary layer, we have to choose $\epsilon \ll \delta$.

In the following we briefly summarize the key ingredients of the boundary layer theory that are needed to provide the necessary information to approximate the cell problem. For this we need to specify the parameters Re , M_∞ and ϵ .

First of all, we note that the pressure change in the boundary layer is negligibly small and, hence, the pressure in the entire flow domain Ω^0 can be considered constant, i.e.,

$$p^0 = p_\infty = \frac{1}{\gamma M_\infty^2}, \quad \left. \frac{\partial^2 p^0}{\partial x_2^2} \right|_{\Gamma_0} = 0. \quad (5.1)$$

Starting point for the derivation of the boundary layer equations is the change of coordinates ⁵:

$$\xi(x_1) := \int_0^{x_1} \rho_\infty u_\infty \eta_\infty d\tilde{x}_1 = \rho_\infty u_\infty \eta_\infty x_1, \quad (5.2)$$

$$\zeta(x_1, x_2) := \sqrt{\frac{Re}{2\xi(x_1)}} \int_0^{x_2} \rho d\tilde{x}_2. \quad (5.3)$$

To describe the boundary layer solution in wall-normal direction, we fix an arbitrary position in streamwise direction, i.e., $\bar{\xi} = \xi(\bar{x}_1)$. Then we define

$$G(\zeta) := \frac{h(x_1(\bar{\xi}), x_2(\bar{\xi}, \zeta))}{h_\infty}, \quad (5.4)$$

where h denotes the mass specific enthalpy (2.5) and determine $F = F(\zeta)$ such that

$$F'(\zeta) = u_1(x_1(\bar{\xi}), x_2(\bar{\xi}, \zeta)). \quad (5.5)$$

Note that (5.1), (5.4) and (2.5) imply

$$\rho = \frac{\rho}{\rho_\infty} = \frac{\rho p_\infty}{\rho_\infty p} = \frac{h_\infty}{h} = \frac{1}{G}. \quad (5.6)$$

The functions F and G satisfy the so-called van Driest equations, cf. ⁵,

$$\begin{aligned} \left(\frac{\eta F''}{G}\right)' + FF'' &= 0, \\ \left(\frac{\eta}{Pr} \frac{G'}{G}\right)' + FG' + \frac{\eta}{h_\infty} \frac{(F'')^2}{G} &= 0 \end{aligned} \quad (5.7)$$

with boundary conditions $F = F' = G' = 0$ at the wall, i.e., $\zeta = 0$, and $F' = G = 1$ at infinity, i.e., $\zeta \rightarrow \infty$. The boundary layer edge or boundary layer thickness δ is defined as the distance to the wall, where the flow velocity reaches 99% of the free-stream velocity. This boundary value problem can be solved by the shooting method, where the second order problem is transformed into an initial value problem for a first order system of ODEs, cf. ⁴¹. Having solved this for F and G , the flow quantities in wall-normal direction can be computed, as sketched in Figure 7 for different positions $\bar{\xi} = 0.25, 0.5, 1$ in streamwise direction.

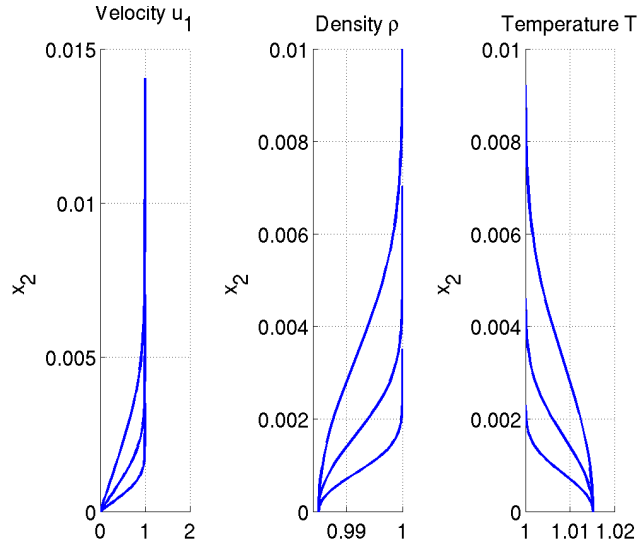


Fig. 7. Boundary layer solution in wall-normal direction for several positions in streamwise direction $\bar{\xi} = 0.25, 0.5, 1$: streamwise velocity u_1 (left), density ρ (middle), temperature T (right).

The zeroth order solution for ρ^0 , u_1^0 is then approximated by evaluating F' and G , respectively, and by (5.5) and (5.6) we compute

$$u_1^0 \approx u_1(\bar{x}_1, x_2) = F'(\zeta(\bar{x}_1, x_2)), \quad \rho^0 \approx \frac{1}{G(\zeta(\bar{x}_1, x_2))}. \quad (5.8)$$

The derivatives $\partial u_1^0/\partial x_2|_{\Gamma_0}$, $\partial^2 \rho^0/\partial x_2^2|_{\Gamma_0}$ at the wall are approximated by evaluating the boundary layer solution at $\zeta = 0$. For this purpose, we calculate from (5.3) the derivative of ζ in wall-normal direction

$$\frac{\partial \zeta}{\partial x_2} = \sqrt{\frac{Re}{2x_1}} \rho = \sqrt{\frac{Re}{2x_1}} \frac{1}{G}. \quad (5.9)$$

Using (5.6) and (5.9) it then follows that

$$\begin{aligned} \frac{\partial \rho}{\partial x_2} &= \frac{\partial}{\partial \zeta} \left(\frac{1}{G(\zeta)} \right) \frac{\partial \zeta}{\partial x_2} = -\sqrt{\frac{Re}{2x_1}} \frac{G'(\zeta)}{G^3(\zeta)}, \\ \frac{\partial^2 \rho}{\partial x_2^2} &= \frac{Re}{2x_1} \frac{1}{(G(\zeta))^4} \left(-G''(\zeta) + 3 \frac{(G'(\zeta))^2}{G(\zeta)} \right). \end{aligned}$$

From this we deduce the approximation

$$\frac{\partial^2 \rho^0}{\partial x_2^2} \Big|_{\Gamma_0} \approx \frac{\partial^2 \rho}{\partial x_2^2}(\bar{x}_1, 0) = \frac{Re}{2\bar{x}_1} \frac{1}{(G(0))^4} \left(-G''(0) + 3 \frac{(G'(0))^2}{G(0)} \right). \quad (5.10)$$

Moreover, using (5.5) and (5.9), it follows that

$$\frac{\partial u_1}{\partial x_2} = \sqrt{\frac{Re}{2x_1}} \frac{F''(\zeta)}{G(\zeta)}.$$

Again in terms of dimensionless variables we obtain the approximation

$$\frac{\partial u_1^0}{\partial x_2} \Big|_{\Gamma_0} \approx \frac{\partial u_1}{\partial x_2}(\bar{x}_1, 0) = \sqrt{\frac{Re}{2\bar{x}_1}} \frac{F''(0)}{G(0)}. \quad (5.11)$$

According to our configuration, sketched in Figure 6, the roughness is located in the interval $I_\epsilon = [0.875, 1]$. In Figure 8 we show how varying the streamwise direction affects the approximations (5.8) of u_1^0 , ρ^0 and (5.10), (5.11) of the derivatives $\partial^2 \rho^0/\partial x_2^2|_{\Gamma_0}$, $\partial u_1^0/\partial x_2|_{\Gamma_0}$, as well as $\partial \rho^0/\partial x_1|_{\Gamma_0}$ and $\partial^2 u_1^0/\partial x_1 \partial x_2|_{\Gamma_0}$, computed using centered finite difference approximations. Obviously, there is only a moderate variation within the range I_ϵ . Therefore, we only use the approximation for fixed $\bar{x}_1 = 1$.

5.2. Numerical solution of the cell problem

For solving the cell problem we have to specify the shape of one element of the periodic roughness defining the boundary W in Figure 5. For our computations we use the C^1 -curve

$$y_2(y_1) := \begin{cases} 1 - r/\epsilon + \sqrt{(r/\epsilon)^2 - (y_1 + \frac{s}{2\epsilon})^2}, & \text{if } y_1 < -\tilde{y}_1, \\ \frac{\tilde{y}_2 - \tilde{y}_2}{-\tilde{y}_1 + \tilde{y}_1} (y_1 + \tilde{y}_1) + \tilde{y}_2, & \text{if } -\tilde{y}_1 < y_1 < -\bar{y}_1 \\ R/\epsilon - \sqrt{(R/\epsilon)^2 - y_1^2}, & \text{if } -\bar{y}_1 < y_1 < \bar{y}_1 \\ \frac{\tilde{y}_2 - \tilde{y}_2}{\tilde{y}_1 - \tilde{y}_1} (y_1 - \tilde{y}_1) + \tilde{y}_2, & \text{if } \bar{y}_1 < y_1 < \tilde{y}_1 \\ 1 - r/\epsilon + \sqrt{(r/\epsilon)^2 - (y_1 - \frac{s}{2\epsilon})^2}, & \text{if } y_1 > \tilde{y}_1 \end{cases} \quad (5.12)$$

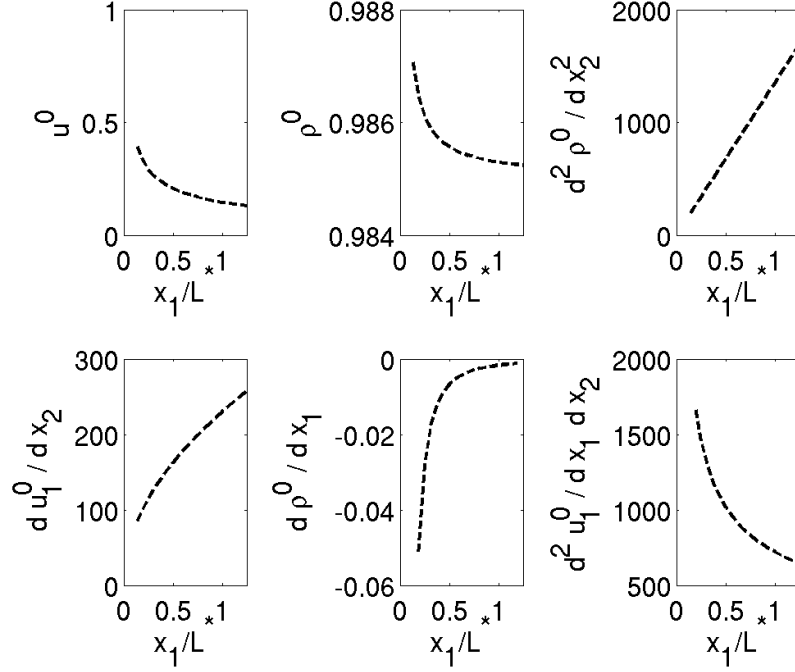


Fig. 8. Variation of zeroth order approximations in streamwise direction on Γ^0 : $u_1^0(\cdot, \epsilon)$, $\rho^0(\cdot, \epsilon)$, $\frac{\partial^2 \rho^0}{\partial x_2^2}(\cdot, 0)$, $\frac{\partial u_1^0}{\partial x_2}(\cdot, 0)$, $\frac{\partial \rho^0}{\partial x_1}(\cdot, 0)$ and $\frac{\partial^2 u_1^0}{\partial x_1 \partial x_2}(\cdot, 0)$.

| | $s = 5\epsilon$ | $s = 10\epsilon$ | $s = 20\epsilon$ |
|------------------------------|------------------|-------------------|---------------------|
| (\bar{y}_1, \bar{y}_2) | (0.441, 0.10249) | (2.1098, 0.28321) | (0.83978, 0.044199) |
| $(\tilde{y}_1, \tilde{y}_2)$ | (2.059, 0.89751) | (4.4726, 0.9292) | (9.7901, 0.98895) |

Table 2. Points (\bar{y}_1, \bar{y}_2) and $(\tilde{y}_1, \tilde{y}_2)$.

characterized by the dimensionless height ϵ and the dimensionless length s , respectively. The parameters r and R typically depend on ϵ and the points (\bar{y}_1, \bar{y}_2) and $(\tilde{y}_1, \tilde{y}_2)$ are chosen such that the curve is C^1 . For our simulations the coordinates of these points are recorded in Table 2.

The shape of this element is depicted in Figure 9. The upper boundary as well

as the periodic boundaries are determined by

$$\begin{aligned}\Gamma_{up} &= \{(y_1, y_2) \in Y : y_1 \in [-s/2, s/2], y_2 = \gamma^y\}, \\ \Gamma_{left} &= \{(y_1, y_2) \in Y : y_1 = -s/2, y_2 \in [y_2(-s/2), 10]\}, \\ \Gamma_{right} &= \{(y_1, y_2) \in Y : y_1 = s/2, y_2 \in [y_2(s/2), 10]\}.\end{aligned}$$

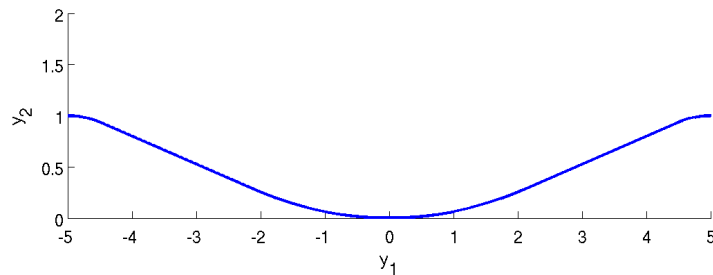


Fig. 9. Shape of one roughness element for $\epsilon = 5 \cdot 10^{-5}/\tilde{L}^*$ and $s = 10\epsilon$, $r = 2\epsilon$, $R = 8\epsilon$.

Here we choose the position of Γ_{up} such that the zeroth order solution in wall normal direction becomes nearly constant. This holds true if $y_2 > \delta(x_1)/\epsilon$, where δ is the boundary layer thickness at x_1 . From Figure 7 we conclude that the value $\bar{x}_2 = 0.01$ for $x_1 = \bar{x}_1 = 1$ is reasonable. Thus $\gamma^y := \frac{\bar{x}_2}{\epsilon}$ becomes 16 and 80 for $\epsilon = 5 \cdot 10^{-5}/\tilde{L}^*$ and $\epsilon = 10^{-5}/\tilde{L}^*$, respectively.

The variational problem (4.8) corresponding to the cell problem is discretized by the Galerkin method using the software deal.II, cf. ⁶: χ is discretized with P2 elements and π and ϕ using P1 elements, respectively. The total number of degrees of freedom is 116546. The linear system is solved using GMRES. Since convection does not dominate diffusion in the cell problem, we don't need to stabilize the discretization. Note that, due to the flat plate assumption, in our test case, the pressure p^0 is constant and thus the pressure derivatives p_1^0 and $p_{1,2}^0$ at the wall drop out in (4.7).

In Figure 10 three configurations are compared for different spacing of the roughness: $s = 5\epsilon, 10\epsilon, 20\epsilon$. The values of the effective constants, defined, accordingly to (4.1), as the mean of χ , ϕ and π on Γ_{up} , are collected in Table 3. It is evident that the shape of the roughness influences the values of the effective constants. In addition we list in Table 4 the mean values for a smaller roughness height ϵ that will be considered later on in our computations as well.

Finally we discuss the influence of the zeroth order solution on the cell problem. Although the zeroth order solution varies strongly over the flow domain, cf. Figure 8, there is only a small influence on the effective constants $\langle \chi \rangle$ and $\langle \pi \rangle$, cf. Figure 11. For $\langle \phi \rangle$ the effect is significant, but it does not enter in the effective problem.

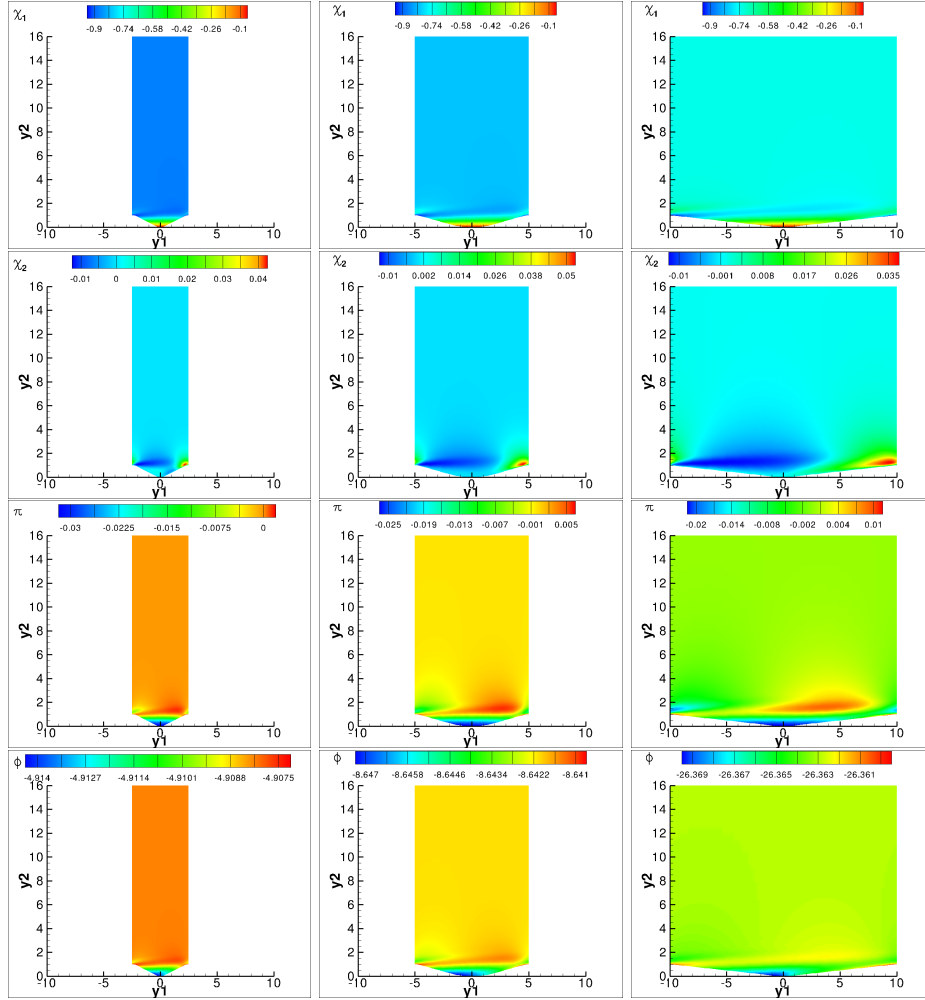


Fig. 10. Solution of the cell problem for $\epsilon = 5 \cdot 10^{-5}/\tilde{L}^*$. First column: $s = 5\epsilon$, second column: $s = 10\epsilon$, third column: $s = 20\epsilon$. First row: χ_1 , second row: χ_2 , third row: π , fourth row: ϕ .

In the incompressible case, Achdou et al. ¹ neglect the transport and the compressibility effects. Doing so as well we end up with the following cell problem of Stokes type

$$\begin{aligned} \nabla_y \cdot \boldsymbol{\chi} &= 0 \text{ in } Y, \\ \eta_\epsilon \Delta_y \boldsymbol{\chi} - \nabla_y \pi &= 0 \text{ in } Y, \end{aligned} \quad (5.13)$$

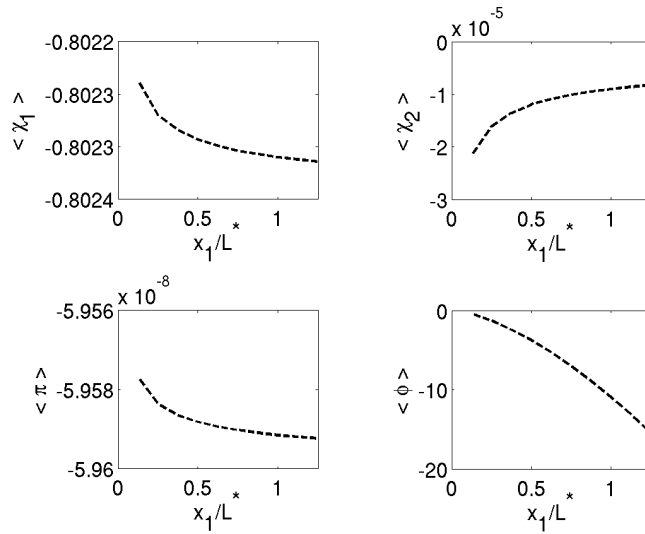
with boundary conditions

$$\begin{aligned} \boldsymbol{\chi} &= -y_2 \mathbf{e}_1 \text{ on } W, \\ (\eta_\epsilon \nabla_y \boldsymbol{\chi} - \pi \mathbb{I}) \mathbf{n} &= \mathbf{0} \text{ on } \Gamma_{up}, \end{aligned} \quad (5.14)$$

| | $s = 5\epsilon$ | $s = 10\epsilon$ | $s = 20\epsilon$ |
|--------------------------|---------------------------|--------------------------|--------------------------|
| $\langle \phi \rangle$ | -4.90814 | -8.64206 | -26.3629 |
| $\langle \pi \rangle$ | $-1.15412 \cdot 10^{-12}$ | $-2.15373 \cdot 10^{-9}$ | $-3.45109 \cdot 10^{-8}$ |
| $\langle \chi_1 \rangle$ | -0.875871 | -0.808255 | -0.730548 |
| $\langle \chi_2 \rangle$ | $-1.41259 \cdot 10^{-5}$ | $-1.03003 \cdot 10^{-5}$ | $-9.09652 \cdot 10^{-6}$ |

 Table 3. Effective constants for $\epsilon = 5 \cdot 10^{-5} / \tilde{L}^*$.

| | $s = 5\epsilon$ | $s = 10\epsilon$ | $s = 20\epsilon$ |
|--------------------------|--------------------------|--------------------------|---------------------------|
| $\langle \phi \rangle$ | -9.7812 | -23.5512 | -101.694 |
| $\langle \pi \rangle$ | $1.16638 \cdot 10^{-9}$ | $4.37567 \cdot 10^{-11}$ | $-3.23961 \cdot 10^{-12}$ |
| $\langle \chi_1 \rangle$ | -0.760638 | -0.632163 | -0.590297 |
| $\langle \chi_2 \rangle$ | $-1.30475 \cdot 10^{-5}$ | $-9.21817 \cdot 10^{-6}$ | $-8.67632 \cdot 10^{-6}$ |

 Table 4. Effective constants for $\epsilon = 10^{-5} / \tilde{L}^*$.

 Fig. 11. Constants $\langle \chi_1 \rangle$, $\langle \chi_2 \rangle$, $\langle \pi \rangle$ and $\langle \phi \rangle$ for different values of x_1 , computed for $\epsilon = 5 \cdot 10^{-5} / \tilde{L}^*$ and $s = 10\epsilon$.

and periodic boundary conditions on Γ_{per} . The numerical solution is shown in Figure 12, for $\epsilon = 5 \cdot 10^{-5} / \tilde{L}^*$ and $s = 10\epsilon$. The corresponding computed effective constants

are

$$\langle \chi_1 \rangle = -0.576257, \quad \langle \chi_2 \rangle = -3.72344 \cdot 10^{-16}, \quad \langle \pi \rangle = -2.90587 \cdot 10^{-19}. \quad (5.15)$$

They strongly differ from the one listed in the second column of Table 3. Thus we conclude that the macroscale quantities cannot be neglected in the compressible case. Later on we will discuss their influence on the effective solution.

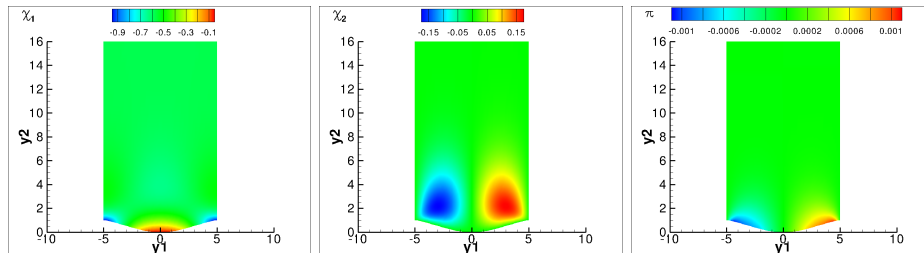


Fig. 12. Solution of the cell problem (5.13), (5.14) for $\epsilon = 5 \cdot 10^{-5}/\tilde{L}^*$, $s = 10\epsilon$: χ_1 (left), χ_2 (center), π (right).

5.3. Numerical solution of the effective problem

Having solved the cell problem and computed the effective constants $\langle \chi \rangle$, we may now solve the effective problem (2.12), (2.13). This is discretized numerically using the solver QUADFLOW¹⁰.

Solver. The QUADFLOW package solves the compressible Navier-Stokes equations using a cell-centered finite volume method on locally refined grids. Mesh adaptation is based on multiscale analysis⁴⁰ instead of classical gradient- or residual-based error estimators. The computational grids are represented by block-structured parametric B-Spline patches³⁵ to deal with complex geometries. In order to reduce the computational load to a tolerable amount, these tools are equipped with parallelization techniques based on space-filling curves¹² to run the simulations on distributed memory architectures.

The convective fluxes are determined by solving quasi-one-dimensional Riemann problems at the cell interfaces. Several approximate Riemann solvers (Roe, HLLC, AUSMDV) and upwind schemes (van Leer) have been incorporated. A linear, multidimensional reconstruction of the conservative variables is applied to increase the spatial accuracy. In order to avoid oscillations in the vicinity of local extrema and discontinuities, limiters with TVD property are used. Concerning the computation of the viscous fluxes, the gradients of the variables at cell interfaces are determined using the divergence theorem. Finally, the time-integration is performed by an explicit multistage Runge-Kutta scheme and a fully implicit Newton-Krylov type method for unsteady and steady state problems, respectively.

For computing a stationary solution with the flow solver, an implicit Euler backward time integration scheme is used with local time steps determined by a global CFL number. The following CFL evolution strategy

$$CFL_{k+1} = \min(CFL_{min} \cdot 1.01^k, CFL_{max}), \quad (5.16)$$

is used with the parameters $CFL_{min} = 0.1$ and $CFL_{max} = 500$ (exact problem) or $CFL_{max} = 100$ (effective problem). Here the index k enumerates the number of time steps since the last grid adaptation, i.e., after each adaptation the CFL number is again set to CFL_{min} . This is essential because by each grid adaptation a perturbation of the steady-state solution corresponding to the old grid is introduced that triggers some unsteady waves on the new grid. When approaching the steady state on a grid, larger CFL numbers are admissible.

In the course of the computation, grid adaptation is applied whenever the averaged density residual has dropped by four orders of magnitude. Note that the first $L - 1$ adaptation steps, where L denotes the number of refinement levels, are only used to generate an initial guess for the iteration on the final adaptive grid. Therefore these have not to be fully converged in time. Since in each adaptation step an additional refinement level can be introduced, the final adaptive grid corresponds to L .

Computations. The effective problem is solved in the domain shown in Figure 6 (right) for different effective constants $\langle \chi \rangle$ corresponding to the roughness determined by (5.12) using the following parameter settings:

$$\begin{aligned} \text{(C1)} \quad \epsilon &= 5 \cdot 10^{-5} / \tilde{L}^*: \quad \text{(a)} \quad s = 10\epsilon, \quad \text{(b)} \quad s = 20\epsilon, \\ \text{(C2)} \quad \epsilon &= 10^{-5} / \tilde{L}^* \quad : \quad \text{(a)} \quad s = 5\epsilon, \quad \text{(b)} \quad s = 10\epsilon. \end{aligned}$$

The effective problem is solved on a smooth domain with boundary Γ_σ on top of the roughness Γ_ϵ , see Fig. 6 (right), with $\sigma = \epsilon$. The boundary portions Σ_0 upstream and downstream of this region are also lifted. For both Γ_σ and Σ_σ we employ the effective boundary conditions with $\langle \chi \rangle \neq \mathbf{0}$ and $\langle \chi \rangle = \mathbf{0}$, respectively. In addition, we compute the solution of the exact problem (2.7), (2.8) on the rough domain, see Figure 6 (left), referred to as *direct numerical simulation* (DNS) where the roughness is fully resolved by the discretization. To appropriately resolve the leading edge of the boundary layer, we add an additional region in front of the plate, where we prescribe symmetry conditions, i.e.,

$$\rho = \rho_\infty, \quad p = p_\infty, \quad u_1 = u_\infty, \quad \frac{\partial u_2}{\partial n} = 0, \quad \text{on} \quad \Sigma_{sym}. \quad (5.17)$$

The DNS and the effective solution are computed using different discretizations. To resolve the roughness in the rough domain we locally need a discretization much smaller than ϵ . On the other hand, for the effective problem on the smooth domain a much coarser discretization is sufficient. For our computations we use $L = 8$ refinement levels, for the exact and the effective problem. For comparison we also

perform computations of the zeroth order problem that corresponds to a flat plate where we replace Γ_ϵ by Γ_0 in Fig. 6 (left).

Flow field. The results of our computations are shown in Fig. 13. First of all we consider the DNS solution, see Figures 13(a), 13(c), 13(e) and 13(g), where we show the streamlines and the streamwise velocity component in a small region near the rough boundary Γ_ϵ . In the sinks of the roughness clockwise-rotating vortices may develop depending on the roughness ϵ and the spacing s . This can best be seen in Fig. 13(a) for large ϵ and small s . However the parallel flow, which is characteristic for a laminar boundary layer, is only perturbed due to the roughness near the wall and, most importantly, stays inside the boundary layer. This can be concluded from the fact that at the boundary layer edge, where the streamwise velocity reaches 99% of the free-stream velocity, the streamlines are horizontal again.

In the effective solution, see Figures 13(b), 13(d), 13(f) and 13(h) the roughness is not resolved. However, comparing the effective solution with the DNS above the roughness shows a similar behavior. To investigate this in more detail we will next compare the results in some cross-section in wall-normal direction.

Wall-normal direction. In order to compare the effective and the exact solution in the boundary layer we introduce the wall shear stress τ_w and the wall shear velocity u_τ

$$\tau_w := \eta_\infty \left. \frac{\partial u_1^0}{\partial x_2} \right|_{\Gamma_0}, \quad u_\tau := \sqrt{\frac{\tau_w}{\rho_\infty}}.$$

Then we define the dimensionless wall distance x_2^+ and the dimensionless streamwise velocity u_1^+ by

$$x_2^+ := \frac{u_\tau}{\nu_\infty} x_2, \quad u_1^+ := \frac{u_1}{u_\tau},$$

where $\nu_\infty = \frac{\eta_\infty}{\rho_\infty}$ denotes the kinematic viscosity coefficient. By means of these quantities the streamwise velocity profile in the boundary layer can be plotted with respect to dimensionless *wall units*.

From our computations we extract data in *wall-normal* direction for the effective problem, the rough problem and the flat plate in wall-normal direction at $x_1 = 0.9375$ that corresponds to the middle of the roughness interval. In Figure 14 we compare the results for $\epsilon = 6.25 \cdot 10^{-4}$ (top), i.e., $\epsilon^+ = 7.0825$, and $\epsilon = 1.25 \cdot 10^{-4}$ (bottom), i.e., $\epsilon^+ = 1.4165$, for different spacings. Note that for *all* computations we use the wall shear stress and the wall shear velocity of the *flat plate* to compute the dimensionless wall distance and velocity. This seems to be reasonable because for vanishing ϵ we expect convergence of the DNS and the effective solution to the flat plate solution.

The vertical lines in the pictures indicate the position of Γ_σ (lower boundary in the effective domain) and Γ_{up} (upper boundary in the cell domain). Here we choose $\gamma = 0.01$, because this corresponds to a position outside the boundary layer of the

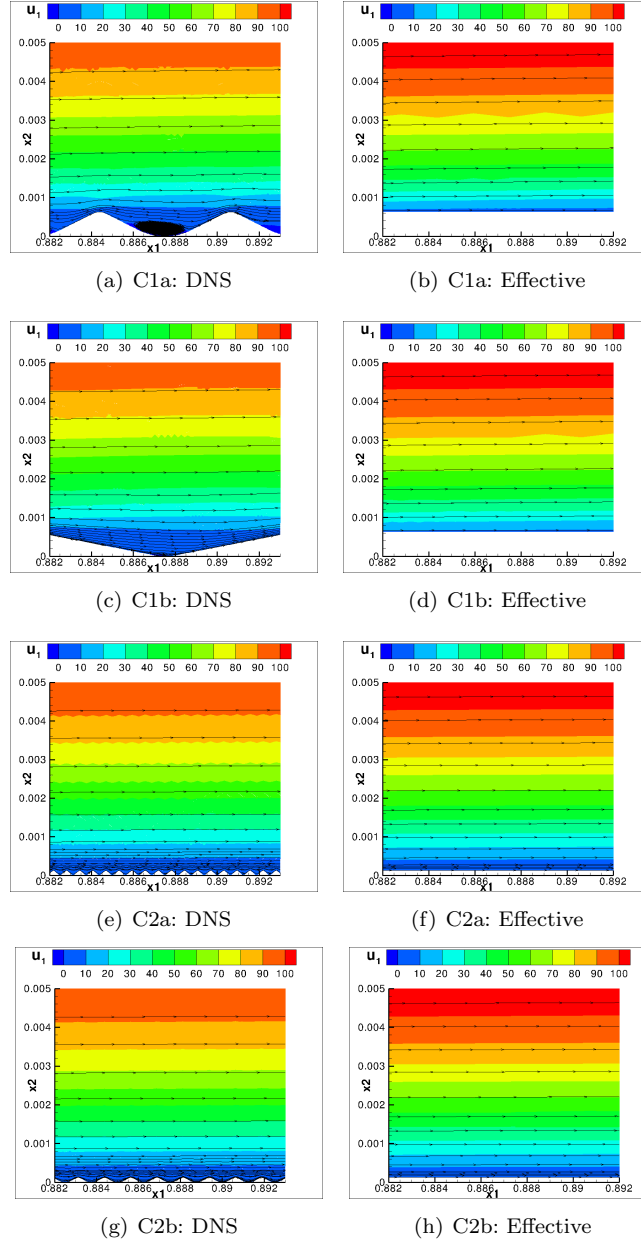


Fig. 13. Streamlines and streamwise velocity component of DNS (left) and effective problem (right).

flat plate solution. Thus in the microscale this becomes $\gamma^y = 16$ and $\gamma^y = 80$ for $\epsilon = 6.25 \cdot 10^{-4}$ and $\epsilon = 1.25 \cdot 10^{-4}$, respectively, characterizing the upper boundary Γ_{up} in the cell domain.

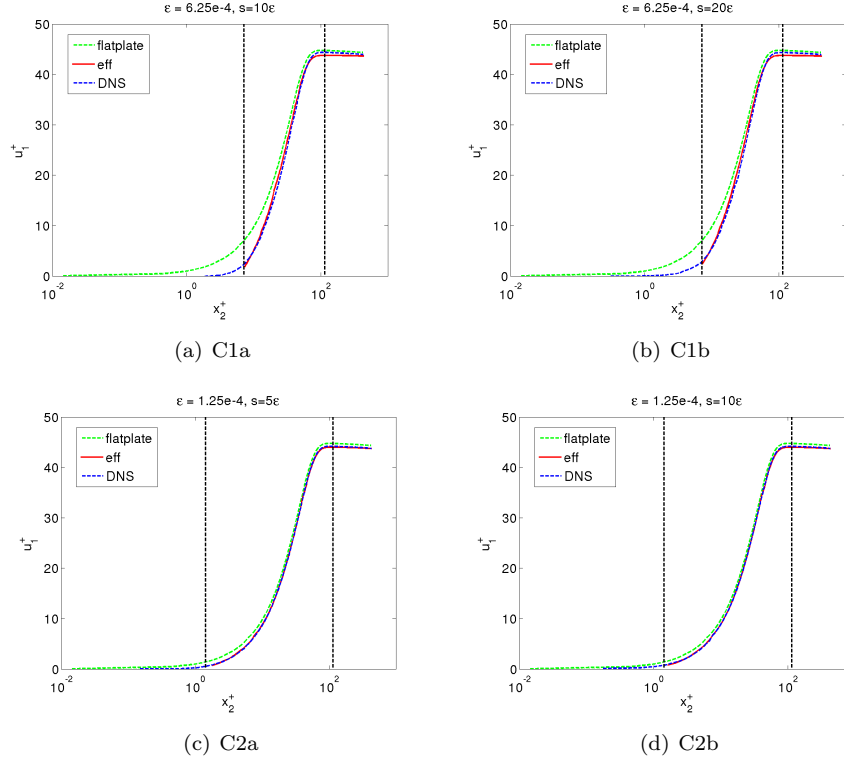


Fig. 14. Streamwise velocity in wall normal direction at $x_1 = 0.9375$ (middle of roughness). The vertical line on the left of each picture is located at $\sigma^+ = \epsilon^+$, the one on the right at $\gamma^+ = 0.01 \frac{u_\tau}{\nu_\infty}$.

There is a good qualitative agreement between the effective solution and the exact solution, for both large and small roughness height and spacing, respectively. We note that for all parameter settings both the DNS $u_1^{\epsilon,+}$ and the effective solution $u_1^{eff,+}$ are close to the flat plate solution $u_1^{0,+} = \frac{u_\infty}{u_\tau} = 44.3303$ in the far field. For decreasing roughness parameter ϵ both the DNS and the effective solution are approaching the solution of the flat plate.

Streamwise direction. In order to further investigate the approximation error we again extract the streamwise velocity component in streamwise direction, i.e., $x_2 = \sigma = \epsilon$, for the flat plate solution u^0 , the DNS solution u^ϵ and the effective solution u^{eff} , see Fig. 15, for $\epsilon = 6.25 \cdot 10^{-4}$ (top) and $\epsilon = 1.25 \cdot 10^{-4}$ (bottom) and different spacings. We observe a good qualitative agreement between the effective and the DNS solution. In particular, the streamwise velocity of the effective solution also decreases on top of the roughness region similar to the exact solution. Furthermore, upstream of the roughness region the velocity in the effective solution and the DNS coincide with the flat plate solution. Downstream the roughness regime we observe

some discrepancy for the larger roughness height, see Figs. 15(a) and 15(b), that reduces with decreasing roughness height, see Figs. 15(c) and 15(d).

In addition, we also computed the effective solution using the cell problem (5.13), (5.14) of Stokes type in ^{1,28,27,23} that does not account for the zeroth order solution u^0 . We note a significant difference in the solutions that underlines the necessity to account for u^0 in the cell problem.

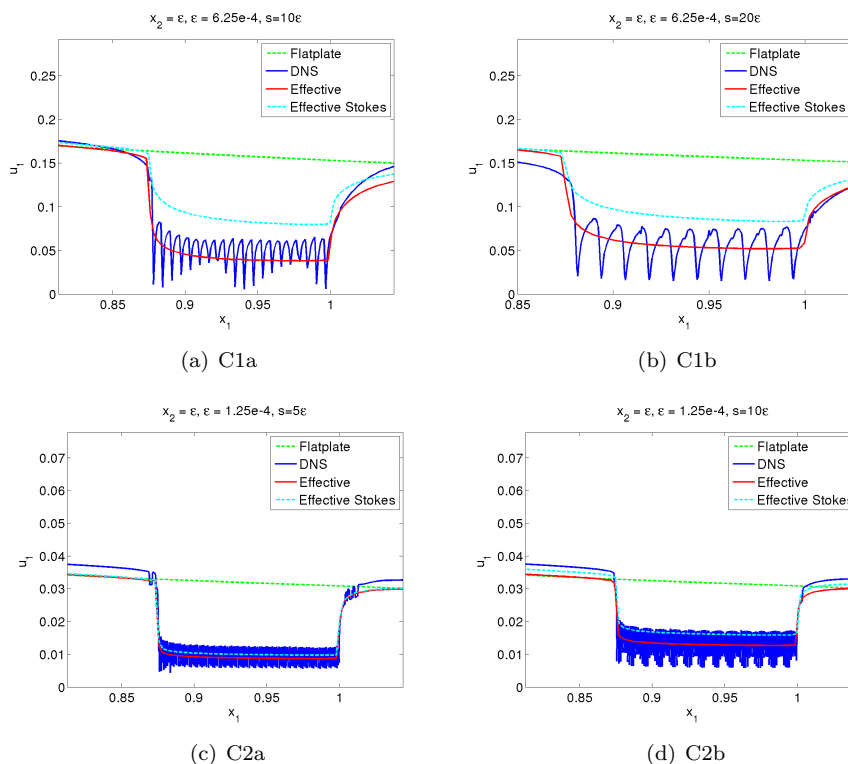


Fig. 15. Streamwise velocity in streamwise direction at $x_2 = \epsilon$.

Skin friction and drag. Now we consider the skin friction coefficient

$$c_f = \frac{\eta \left(\frac{\partial u_1}{\partial x_2} - \frac{\partial u_2}{\partial x_1} \right)}{0.5 \rho_\infty u_\infty^2} = \tilde{c}_f Re$$

at the wall. It is shown in Figures 16 for the DNS, the effective solution and the zeroth order solution for a flat plate. For the DNS we observe an oscillating behavior on top of the roughness, where the skin friction reduces above the sinks and increases again at the elevations because the flow is locally expanding or compressing. Typically, the skin friction is smaller with increasing spacing s and decreasing

height ϵ , respectively. At the leading edge of the roughness it is higher, because there the unperturbed flow hits the obstacle first. For the effective solution we observe a similar behavior but without oscillations. It stays between the maximum and minimum values of the DNS, but above the similarity solution of the flat plate. From the skin friction coefficient we compute the aerodynamic drag coefficient

$$c_D = \frac{1}{|\Gamma|} \oint_{\Gamma} c_f (n_2 \cos(\alpha) - n_1 \sin(\alpha)) + (p - p_{\infty}) (n_1 \cos(\alpha) + n_2 \sin(\alpha)) dA = \tilde{c}_D Re.$$

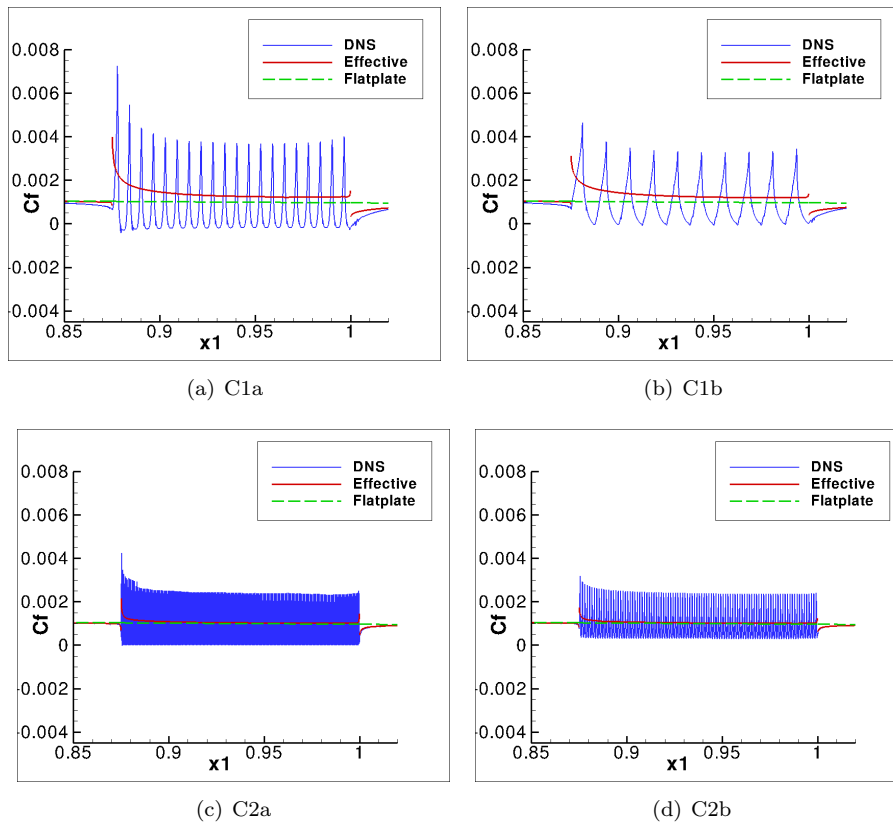
For the DNS ($\Gamma = \Gamma_{\epsilon} \cup \Sigma_0$) and the effective solution ($\Gamma = \Gamma_{\sigma} \cup \Sigma_{\sigma}$) the values are listed in Table 5. For the flat plate ($\Gamma = \Gamma_0 \cup \Sigma_0$) we obtain $c_D = 1.224175 \cdot 10^{-3}$ determined by the Quadflow computation for the flat plate. We note that both the effective solution and the DNS solution show a smaller value for the drag coefficient than the flat plate solution. On top of the roughness the streamwise velocity decreases, see Fig. 15. Thus, the velocity gradient in wall-normal direction is reduced resulting in a smaller skin friction.

Note that the optimization of the roughness structure is beyond the scope of this work. Related work in this regard for incompressible, laminar flows can be found in 22.

| | (C1a) | (C1b) | (C2a) | (C2b) |
|------------|--------------------------|--------------------------|--------------------------|--------------------------|
| DNS | $1.15799 \cdot 10^{-3}$ | $1.189287 \cdot 10^{-3}$ | $1.218292 \cdot 10^{-3}$ | $1.206932 \cdot 10^{-3}$ |
| Effective | $1.159905 \cdot 10^{-3}$ | $1.159265 \cdot 10^{-3}$ | $1.216035 \cdot 10^{-3}$ | $1.21596 \cdot 10^{-3}$ |
| flat plate | $1.224175 \cdot 10^{-3}$ | $1.224175 \cdot 10^{-3}$ | $1.224175 \cdot 10^{-3}$ | $1.224175 \cdot 10^{-3}$ |

Table 5. Aerodynamic drag coefficient due to friction c_D for DNS, effective solution and flat plate solution.

Computational effort. Finally we discuss the efficiency of the effective solution in comparison to the DNS. For this purpose we summarize in Table 6 (left) the number of cells in the block $B^{\sigma} = [0.875, 1] \times [\sigma, 0.0375]$ and $B^{\epsilon} = [0.875, 1] \times [0, 0.0375] \cap \Omega^{\epsilon}$ sitting on top of Γ_{σ} and Γ_{ϵ} , respectively. Note that in the remaining computational domain $\Omega^{\sigma} \setminus B^{\sigma}$ and $\Omega^{\epsilon} \setminus B^{\epsilon}$ the resolution is similar for the effective simulation and the DNS, respectively, because there is no roughness but a flat plate. We note that the computational load for the DNS is significantly higher than for the effective solution, because the roughness requires a much finer grid near the boundary Γ_{ϵ} than for Γ_{σ} . In particular, when ϵ is smaller, see the first row in Table 6 (left), the effective solution becomes increasingly efficient. Note that the number of roughness elements to be resolved on Γ_{ϵ} varies significantly, see Table 6 (right). On the other hand, we can predict by the cheaper effective solution reasonable approximations for the local skin friction coefficient and the aerodynamic drag coefficient *without* resolving all small scale effects but taking into account their effect on macroscale variables such as averages just by effective boundary conditions.


 Fig. 16. Skin friction coefficient c_f for DNS, effective solution and flat plate solution.

| | (C1a) | (C1b) | (C2a) | (C2b) | | (C1) | (C2) |
|------------|-------|-------|--------|-------|-----|------|------|
| DNS | 59736 | 53469 | 133587 | 72771 | (a) | 20 | 200 |
| Effective | 10924 | 10978 | 11104 | 11098 | (b) | 10 | 100 |
| flat plate | 3118 | 3118 | 3118 | 3118 | | | |

 Table 6. Number of cells of the final grid in $[0, 875, 1] \times [0, 0.0375]$ for DNS, effective solution and flat plate solution; number of roughness elements on Γ_ϵ (right).

6. Conclusions

In this paper the ideas of Achdou et al. ¹ for incompressible low Reynolds number flow have been adapted to the more complex mathematical model of the compressible Navier-Stokes equations. The zeroth order problem is approximated by van Driest's similarity solution for the laminar compressible boundary layer of a flat plate. From this we compute the macro-scale parameters involved in the cell problem on the micro scale. In principle, we have to solve the cell problem whenever

we evaluate the effective boundary conditions when solving the effective problem. To avoid this we may determine for the solution of the cell problem a parameter dependent representation where we apply, for instance, reduced basis methods in a precomputation state. Averaging the solution of the cell problem provides us with the effective constant that characterizes the Navier wall law in the effective problem on the smooth domain.

In future work we will investigate laminar as well as turbulent flows over riblet structures in three dimensions. In contrast to the two-dimensional configuration considered in the present work the roughness will be aligned in spanwise direction instead of streamwise direction. This configuration is certainly more appropriate to reduce drag by influencing turbulence structures near the surface. This technology might be useful for increasing the efficiency of airplanes with regard to energy consumption by mounting riblet structures to the airplane wings. Alternatively, one might think of high-frequency waves actuated in spanwise direction on the surface of an airplane. Experimental as well as numerical investigations for simple generic configurations in case of riblets^{33,24,22} and surface waves^{32,17,18} are promising although most of the investigations have been performed for incompressible flow.

Acknowledgment

This work has been performed with funding of the German Research Council (DFG) within the DFG Research Unit FOR 1779 by grant DA 117/22-1 and the DFG Collaborative Research Center SFB-TR-40.

The authors would like to thank Christian Windisch for implementing the effective boundary conditions in QUADFLOW, generating grids and performing DNS for the rough problem.

References

1. Y. Achdou, O. Pironneau, F. Valentin, “Effective boundary conditions for laminar flows over periodic rough boundaries”, *J. Comp. Phys.*, **147**, 187–218, 1998.
2. Y. Achdou, O. Pironneau, F. Valentin, “New wall laws for unsteady incompressible Navier-Stokes equations”, *ECCOMAS 2000*, 2000.
3. Y. Achdou, P. Le Tallec, F. Valentin, O. Pironneau, “Constructing wall laws with domain decomposition or asymptotic expansion techniques”, *Comput. Methods Appl. Mech. Engrg.*, **151**, 215–232, 1998.
4. Y. Achdou, O. Pironneau, F. Valentin, “Comparison of wall laws for unsteady incompressible Navier-Stokes equations”, *First MIT Conference on Computational Fluid and Solid Mechanics, Boston, USA, June 12-15*, 2001.
5. J.D. Anderson, “Hypersonic and high temperature gas dynamics”, *McGraw-Hill Series in Aeronautical and Aerospace Engineering*, 1989.
6. W. Bangerth, R. Hartmann, G. Kanschat, “deal.II — a general-purpose object-oriented finite element library”, *ACM Trans. Math. Softw.*, **33(4)**, 24/1–24/27, 2007.
7. G.R. Barrenea, P. Le Tallec, F. Valentin, “New wall laws for the unsteady incompressible Navier-Stokes equations on rough domains”, *Mathematical Modeling and Numerical Analysis*, **36**, 177–203, 2002.

8. A. Basson, D. Gerard-Varet, “Wall laws for fluid flows at a boundary with random roughness”, *Commun. Pure Appl. Math.*, **61**, 941–987, 2008.
9. G.S. Beavers, D.D Joseph, “Boundary conditions at a naturally permeable wall”, *J. Fluid Mech.*, **30**, 197–207, 1967.
10. F. Bramkamp, Ph. Lamby, S. Müller, “An adaptive multiscale finite volume solver for unsteady and steady state flow computations”, *J. Comp. Phys.*, **197(2)**, 460–490, 2004.
11. A. Bensoussan, J.L. Lions, G. Papanicolaou, “Asymptotic analysis for periodic structures”, North-Holland, Amsterdam, 1978.
12. K. Brix, S. Mogosan, S. Müller, G. Schieffer, “Parallelization of multiscale-based grid adaptation using space-filling curves”, in *Multiresolution and Adaptive Methods for Convection-Dominated Problems*, F. Coquel, Y. Maday, S. Müller, M. Postel, Q.H. Tran (eds.), *ESAIM:Proceedings*, **29**, 108–129, 2009.
13. D. Bresch, V. Milisic, “High order multi-scale wall-laws, Part I: the periodic case”, *Quarterly of Applied Mathematics*, **68**, 229–253, 2010.
14. D. Bresch, V. Milisic, “Towards implicit multi-scale wall-laws”, *Comptes Rendus Mathématique*, **346**, 833–838, 2008.
15. D.M. Bushnell, K.J. Moore, “Drag reduction in nature”, *Ann. Rev. Fluid Mech.*, **23**, 65–79, 1991.
16. J. Casado-Diaz, E. Fernandez-Cara, J. Simon, “Why viscous fluids adhere to rugose walls: a mathematical explanation”, *J. Differential Equations*, **189**, 526–537, 2003.
17. Y. Du, G.E. Karniadakis, “Suppressing wall turbulence by means of a transverse traveling wave”, *Science* **288**, 1230–1234, 2000.
18. Y. Du, G.E. Karniadakis, “Drag reduction in wall bounded turbulence via a transverse traveling wave”, *J. Fluid. Mech.* **457**, 1–34, 2002.
19. Y. Efendiev, T.Y. Hou, “Multiscale Finite Element Methods: Theory and Applications”, Springer, 2009.
20. W. E, B. Engquist, “The heterogeneous multiscale methods”, *Commun. Math. Sci.* **1(1)**, 87–132, 2003.
21. W. E, B. Engquist, “The heterogeneous multi-scale method for homogenization problems”, in *Multiscale Methods in Science and Engineering*, 89–110, Lecture Notes Comput. Sci. Eng., Vol. 44, Springer, Berlin, 2005.
22. E. Friedmann, “The Optimal Shape of Riblets in the Viscous Sublayer”, *J. Math. Fluid Mech.*, **12**, 243–265, 2010.
23. E. Friedmann, Th. Richter, “Optimal microstructures drag reducing mechanism of riblets”, *Journal of Mathematical Fluid Mechanics* **13**, 429–447, 2011.
24. K. Iwamoto, K. Fukagata, N. Kasagi, Y. Suzuki, “Friction drag reduction achievable by near-wall turbulence manipulation at high Reynolds numbers”, *Physics of Fluids* **17**, 011702, doi:10.1063/1.1827276, 2005.
25. J. Kevorkian, J.D. Cole, “Perturbation methods in applied mathematics”, Applied Mathematical Sciences, Vol. 34. New York-Heidelberg-Berlin: Springer-Verlag, 1981.
26. W. Jäger und A. Mikelic, “On the boundary conditions at the contact interface between a porous medium and a free fluid”, *Ann. Scuola Norm. Sup. Pisa Cl. Sci.*, **23**, 403–465, 1996.
27. W. Jäger, A. Mikelic, “On the interface boundary conditions of Beavers, Joseph and Saffman”, *SIAM J. Appl. Math.*, **60**, 1111–1127, 2000.
28. W. Jäger, A. Mikelic, “On the roughness-induced effective boundary conditions for an incompressible viscous flow”, *Journal of Differential Equations*, **170**, 96–122, 2001.
29. W. Jäger, A. Mikelic, N. Neuss, “Asymptotic analysis of the laminar viscous flow over a porous bed”, *SIAM J. Sci. Comput.*, **22**, 2006–2028, 2001.

30. W. Jäger, A. Mikelic, “Couette flows over a rough boundary and drag reduction”, *Commun. Math. Phys.*, **232**, 429–455, 2003.
31. V. Jikov, S. Kozlov, O. Oleinik, “Homogenization of differential operators and integral functionals”, Springer, Berlin, 1995.
32. W.J. Jung, N. Mangiavacchi, R. Akhavan, “Suppression of turbulence in wall-bounded flows by high frequency spanwise oscillations”, *Physics of Fluids A* **4**, 1605–1607, 1992.
33. S. Kang, H. Choi, “Active wall motions for skin-friction drag reduction”, *Physics of Fluids* **12**, 3301–3304, 2000.
34. J.R. Kweon, R.B. Kellogg, “Regularity of solutions to the Navier-Stokes system for compressible flows on a polygon”, *SIAM J. Math. Anal.* **35(6)**, 1451–1485, 2004.
35. Ph. Lamby, “Parametric multi-block grid generation and application to adaptive flow simulations”, Diss. RWTH Aachen, 2007.
36. P. Luchini, “Linearized no-slip boundary conditions at a rough surface”, *J. Fluid Mech.*, **737**, 349–367, 2013.
37. A. Madureira, F. Valentin, “Asymptotics of the Poisson problem in domains with curved rough boundaries”, *SIAM J. Math. Anal.*, **38**, 1450–1473, 2006/07.
38. A. Mikelic, “Rough boundaries and wall laws” , in Qualitative properties of solutions to partial differential equations, *Lecture Notes of Necas Center for Mathematical Modeling*, edited by E. Feireisl, P. Kaplicky and J. Malek, **5**, 103–134, 2009.
39. B. Mohammadi, O. Pironneau, F. Valentin, “Rough boundaries and wall laws”, *Int. J. Numer. Meth. Fluids*, **27**, 169–177, 1998.
40. S. Müller, “Adaptive multiscale schemes for conservation laws”, *Lecture Notes on Computational Science and Engineering*, Vol. 27, first ed., Springer Verlag, 2003.
41. G. Palmer, “Technical Java”, Prentice Hall, 2003.
42. M.P. Schultz, K.A. Flack, “The rough-wall turbulent boundary layer from the hydraulically smooth to the fully rough regime”, *J. Fluid Mech.*, **580**, 381–405, 2007.
43. L. Tartar, “The general theory of homogenization. A personalized introduction”, *Lecture Notes of the Unione Matematica Italiana*, 7. Springer-Verlag, Berlin; UMI, Bologna, 2009.
44. S. Veran, Y. Aspa, M. Quintard, “Effective boundary conditions for rough reactive walls in laminar boundary layers”, *Int. J. Heat Mass Transfer*, **52**, 3712–3725, 2009.